Automated 3D reconstruction of Lodox Statscan images for forensic application

SUBMITTED TO THE UNIVERSITY OF CAPE TOWN
In partial fulfillment of the requirements
for the degree of Master of Science in Medicine,
in Biomedical Engineering
2010

Frank Bolton

23 July 2011

Declaration

1. I know that plagiarism is wrong. Plagiarism is to use another's work and pretend that it is one's own.

2. I have used the Harvard convention for citation and referencing. Each contribution to, and quotation in, this thesis from the work(s) of other people has been attributed, and has been cited and referenced.

3. This thesis is my own work.

4. I have not allowed, and will not allow, anyone to copy my work with the intention of passing it off as his or her own work.

5. I acknowledge that copying someone else's assignment or essay, or part of it, is wrong, and declare that this is my own work.

Signature _

Acknowledgments

Abstract

The main objectives of this project are to perform tomographic reconstruction with manually scanned projection data from a Lodox Statscan full body digital radiography system, and to produce tools to allow automated generation of information required to perform the tomographic reconstruction.

The Lodox Statscan has a general geometry that is different from that of a conventional CT scanner, and geometric measurements of the Lodox Statscan need to be generated from image data in order to perform tomographic reconstruction. To find these measurements, a software-based model of the Lodox Scatscan projection geometry, three calibration points forming a calibration object that is included in all of the projections, and a reprojection-error least-cost optimisation are used. A method is developed that transforms the Lodox data into orthogonal parallel beam projection data, on which a filtered back-projection is performed, producing tomographic reconstructions.

Automated image analysis components work well most of the time, with manual annotation of features required for 4% of the image data. The reconstructions of a head phantom are successful and show anatomical detail with reconstructions showing good spatial accuracy (spatial resolution of the reconstructions was low). Reprojection of the reconstruction verified that the reconstructions are successful.

As a research tool, the methods produced show merit. Some work is needed, though, before commercial implementation is feasible.

Contents

Glossary

Anteroposterior   From front to back.

Binning   Image resolution reduction where the resolution is reduced, but the signal to noise ratio is increased. Perfomed by adding pixel intensity values together.

CCD   Charged-coupled device, the semiconductor type used in many cameras.

CT   Computed tomography.

Dead man's switch   A switch that needs to be activated the entire time that a process takes place. Releasing the switch signals a problem and the system must revert to a safe, stationary state.

DICOM   The Digital Imaging and Communications in Medicine (DICOM) Standard.

HMI   Human machine interface. The software application that allows the user to set up machine parameters and monitor the machine state.

MRI   Magnetic resonance imaging.

Phantom   Specially designed test objects used in medical imaging. May be made to mimic human tissue or have a specific size and material composition.

SCADA   Supervisory control and data acquisition. Software that allows a user to monitor and control a process using a graphical representation of the process or parts of the process.

Supine   Lying down on one's back, with the face up.

C-arm   The component on the Lodox Statscan mechanical assembly that holds both the X-ray source and the detector.

Chapter 1

Introduction

The Lodox Statscan, Computed Tomography (CT) and previous work using the Lodox Statscan for tomographic reconstruction are introduced, as well as an explanation of the directional terms used for describing the position of objects on the scan table as well as the on a projection image.

The Lodox Statscan is a full body linear slot scanning digital X-ray machine. There are two Lodox X-ray machines operational at forensic science Laboratories in South Africa. CT reconstruction using images produced by the Lodox Statscan had previously been explored.

This project is about producing 3D tomographic reconstructions using Lodox images using automated image processing procedures, and in a more reproducible way than has been implemented previously for use in forensic science cases. Lodox system characteristics limit the rate at which scanning can take place, forcing the procedure to take too long for Lodox based medical computed tomography to be feasible.

1.1   X-ray in forensic science

X-ray imaging is used routinely in forensic science. The images are mainly used to find projectiles for ballistic investigations and to identify fractures.

Problems with using conventional cone-beam X-ray machines for forensic science are that multiple scans are required to image the entire body and is that it is easy to miss a projectile in a region that is not captured in any of the images.
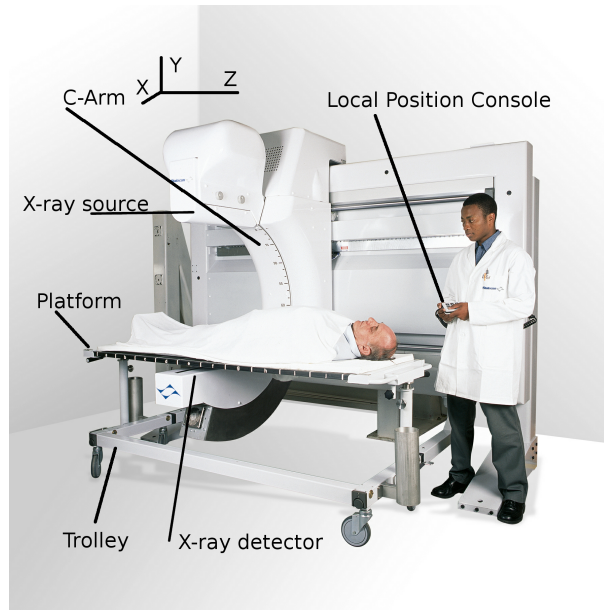
Figure 1.1: Relevant components making up the Lodox Statscan.

1.2 Computed tomography in forensic science

Computed tomography is an imaging technique where an object is scanned from many different angles using X-rays and, using the set of X-ray projections, a tomographic reconstruction algorithm generates a cross-sectional "slice" view of the object. These cross-sectional views of the object provide diagnostic information not visible in projections and can form part of three-dimensional volume reconstructions.

Computed tomography has been used extensively for medical cases, and having been proven to have value in the medicolegal domain, is being adopted for use in post-mortem autopsy procedures. CT has not penetrated the forensic science market as well as it penetrated the medical market.

1.3 Lodox

The Lodox Statscan is a full body digital X-ray machine developed and manufactured by the South African company, Lodox Systems. It was designed with the objective of generating high quality, low dose, full body X-ray images of trauma patients with life threatening injuries in emergency rooms (Beningfield et al., 2003). The Lodox Statscan is shown in Figure 1.1 and an example X-ray image generated using the Lodox Statscan is shown in Figure 1.2.

There are Lodox X-ray machines installed at the two forensic science laboratories in the Western Cape in South Africa.

Figure 1.2: Lodox Anteroposterior X-ray image.
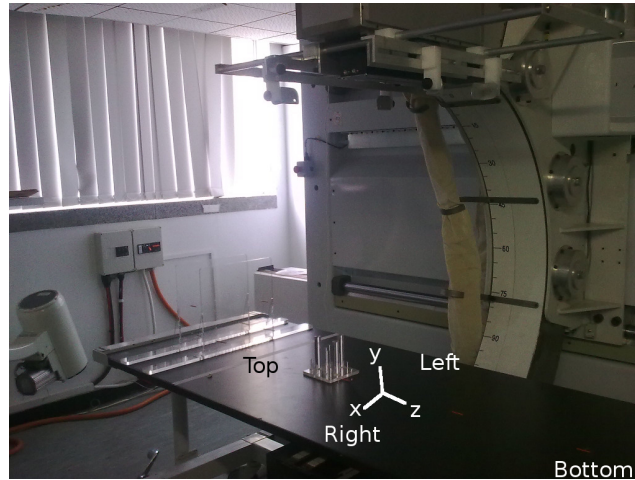
Figure 1.3: Physical locations and directions of objects scanned in the Lodox.

1.3.1   Navigating around the Lodox Statscan

X-ray imaging is projective, which means that a three-dimensional object is collapsed into a two-dimensional image. The angle at which the Lodox X-ray machine scans the object is set by the operator. A three-dimensional coordinate frame is required to describe the location of a point being imaged, and the position and orientation of the coordinate system and the position of the point are considered stationary throughout the scanning procedure. A two-dimensional coordinate set is required to describe the projection of the point onto the image. This coordinate system is defined by the plane traced out by the detector as a particular projection is generated, and is considered to vary with the changing of the c-arm angle.

Describing the regions of a physical object that is being scanned corresponds to describing the regions of a patient on the trolley (Figure 1.3). Top is where the patient's head would normally be and is where the scan usually starts. Left, right are where the patient's left and right sides would be and bottom is where the patient's feet would be. The c-arm moves from top to bottom whilst performing an X-ray scan. A third direction pair, anterior and posterior, will be defined for a supine patient. A left-handed Cartesian coordinate system is defined such that the +z direction is defined as the downward direction and is in the scanning direction, the +x direction is defined as pointing right and the +y direction is defined to be a vertical line perpendicular to (and pointing out of) the table.

In an anteroposterior X-ray image, describing the regions of the patient is done with directions top, bottom, left and right relative to the subject. In a lateral X-ray image, directions top and bottom remain valid, the left hand side of the image is the patient's posterior side and the right hand side of the image is the patient's anterior side.

1.4 Computed tomography using the Lodox Statscan

Tomographic reconstruction using Lodox images has been investigated (de Villiers, 2000, 2004) and has been used to generate magnification distortion corrected X-ray images (Beets, 2007).

While these investigations yielded successful reconstructions, challenges were encountered that prevented the Lodox CT from being feasible as an academic tool or a commercial product.

Some of the problems that were encountered during the previous Lodox tomography studies have been solved through Lodox Statscan development, namely erratic occurrence of low quality images and camera overlap artifacts. The main existing challenge is to provide a reliable and reproducible way to compensate for the Lodox Statscan's geometry. Other limitations that still need solving are:

- a limited number of c-arm angles that are practically measurable as the scanning is done manually,

- the X-ray image start position varies between images even though the Lodox Statscan is given a constant starting set-point,

- operator intensive processes are required to move, pre-process, and reconstruct image data,

- slow computation of the reprojection and the reconstruction images.

The Lodox Statscan design focused on two scanning procedures, anteroposterior imaging and lateral imaging. The point about which the c-arm rotates (the centre of rotation) was placed accordingly (Figure 1.4), providing good imaging and taking up as little space in the emergency room as possible. This is significantly different to the mechanical configuration of a conventional CT scanner (Figure 1.5).

Mechanical limitations prevent the Lodox Statscan from being able to generate projection data as quickly as a commercial CT scanner, and it will never generate projection data for reconstruction quickly enough to image an unrestrained live patient without introducing motion artifacts.

The use of Lodox images for forensic tomographic reconstruction is more feasible and this makes extending the knowledge in the field and producing more reliable methods worthwhile.

1.5 Project overview

The functionality produced in this project focusses on providing forensic science laboratories with useful reconstruction images.
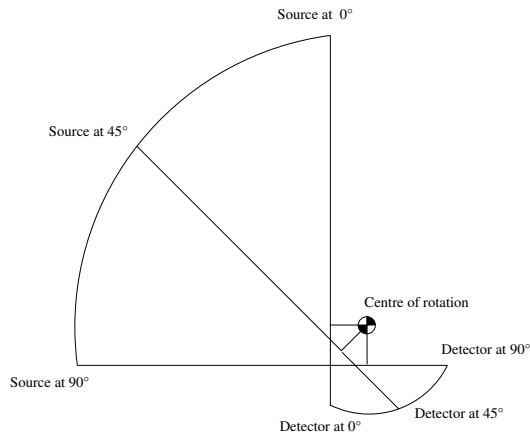
Figure 1.4: Rotation of Lodox Statscan.
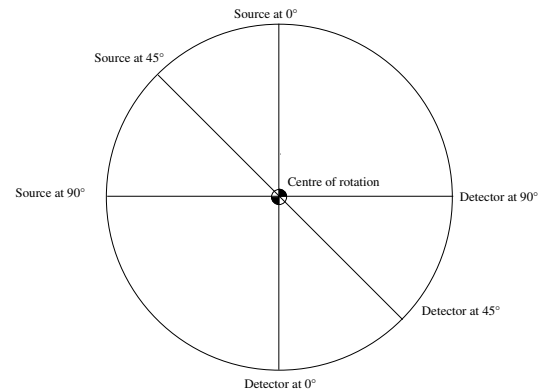
Figure 1.5: Rotation of a conventional CT scanner.

1.5.1   Problem statement

The Lodox Statscan has a peculiar geometry. In order to generate tomographic reconstruction images, the Lodox projection data is transformed to match an orthogonal beam projection set. This transformation is derived in this project, as well as a method for generating the parameters it requires from a set of Lodox Statscan images. Tomographic reconstruction of the orthogonal projection data is then performed.

1.5.2   Objectives

The following were the objectives of this project:

- Manually scan a set of X-ray images for tomographic reconstruction.

- Produce a hardware and automatic software system that will reliably and reproducibly correct for the varying start positions for a set of scans.

- Produce a hardware and automatic software system that will reliably and reproducibly estimate the Lodox Statscan geometry and the c-arm angles for a set of scans.

- Using C++, automate the image retrieval from the proprietary Lodox database and export projection files in a DICOM format.

- Generate tomographic reconstructions using a set of scans.

- Produce quantitative results of how well the reconstruction performs.

1.5.3   Scope and limitations

Only one set of projections was used in this investigation. The Lodox Statscan machine available for this investigation was out of order for at least 6 months. When it finally was available, it was not fully operational and suffered intermittent problems. This meant that scanning took extra time and at this stage more time could not be committed to generating projection data. Subsequent to this study, the AMI Lodox Statscan underwent a significant overhaul.

For full tomographic reconstruction, 180° worth of orthogonal projection data is required. The Lodox Statscan has an angular scan range of $0° \rightarrow 90°$. To generate sufficient projection data, 2 sets of scans are performed with the trolley rotated in between the two sets. The set scanned first is considered upright and is referred to as the first set. The set scanned second is considered upside down and is referred to as the second set.

Slice image reconstructed is performed at 512×512 pixel resolution.

The image processing and reconstructions are performed using MATLAB and the image processing and optimisation toolboxes.

1.6   Layout and overview

1.6.1   Chapter 2

A review of the relevant literature is presented as well as an investigation into fundamental theory: the mathematics and transforms required to produce tomographic reconstructions.

The medicolegal autopsy, an important procedure in forensic science, is introduced. The Lodox Statscan and computed tomography are investigated more formally, with the mathematical transforms for converting Lodox projection data into a format useful for tomographic reconstruction derived.

1.6.2   Chapter 3

A detailed design of the system is made, with the individual components used explained in the order that they are applied to the projection image data. These include the techniques used to correct for the imprecise start position of the scanning, parameter estimation, image transformation, and image reconstruction.

1.6.3 Chapter 4

Performance measurement experiments are defined, testing both the sub-system level components as well as the overall image reconstruction system.

Experimental results produced are also presented and discussed.

1.6.4 Chapter 5

Concluding remarks are made and recommendations for future work are provided.

Chapter 2

Literature review and relevant theory

This investigation applies tomographic reconstruction to images generated using a Lodox Statscan with the objective of producing tools that could eventually provide forensic science laboratories with useful reconstruction images. The Medicolegal autopsy is introduced as it is an important procedure used in forensic science. The use of X-ray imaging and Computed Tomography in the autopsy are covered.

The company Lodox and the Lodox Statscan are introduced as background information on the device history and the use of the Lodox Statscan in both clinical and forensic environments.

The mathematics of computed tomography is investigated. This serves to introduce the background theory, to set the context for the derivation of the Lodox specific transformations, and to establish notation.

Modern topics in the field of tomographic imaging are introduced, as well as how they could fit in with Lodox tomography.

2.1   Medicolegal autopsy

Postmortem examinations in forensic pathology make use of autopsies during which a cadaver is dissected to gain knowledge regarding the cause of and the conditions surrounding a sudden, unexpected or suspicious death. X-ray imaging is used routinely in autopsies and computed tomography to a lesser degree.

Two Lodox X-ray machines are currently used to produce X-ray images for autopsies in South Africa, and as Lodox generated image data has been used previously to produce tomographic images, a case is presented for extending Lodox tomography towards a solution that can be implemented for use by forensic scientists in postmortem studies.

2.1.1 Postmortem examinations and 3D medical imaging

As the Lodox X-ray machines are currently used to produce X-rays for postmortem use, other medical devices applied to forensics are of interest.

Shortly after X-ray technology was first made available for clinical use, it was adopted into the field of forensic pathology (Poulsen and Simonsen, 2007). Advanced 3D imaging techniques such as computed tomography (CT) and magnetic resonance imaging (MRI) have also been adopted into the field of forensic pathology, albeit at a much slower rate. Some reasons why these 3D imaging technologies have not penetrated the market effectively are the high cost of the advanced imaging hardware and the high level of training that is required to operate the equipment. The main thrust to include advanced imaging techniques in forensic pathology is from a Swiss research group (Thali et al., 2007) with their Virtopsy project. They aim to prove that a set of digital scans can provide enough information to make postmortem dissections unnecessary. At present, the forensic science community is happy to make use of the information that advanced imaging systems can provide, but are not yet confident that the axial slice images may rule out the need to dissect (O'Donnell and Woodford, 2008). Pathologies that can be identified with the help of volume reconstructions or axial slice images include gunshot trauma, haematoma, tension pneumothorax (possibly with an associated mediastinal shift), fractures, strangulation, and detection of foreign bodies and air embolisms (Thomsen et al., 2009; Gibb, 2008; Jeffery et al., 2008; Bolliger et al., 2008). Many of these can be missed easily or altogether masked with dissection alone (Thomsen et al., 2009).

2.1.2 Forensic application of computed tomography

Computed tomography scanners are widely used in hospitals and the technology is well established. It would seem logical that this technology would have been readily adopted for forensic science but this has not not been the case. Although there was a case in the late 1970's where CT was used to describe a gunshot to the head (Bolliger et al., 2008), the rate of use of CT in forensics is low mainly because of a lack of awareness in the forensic community of the potential of cross-sectional imaging (Thali et al., 2007).

2.2 Lodox Statscan

Lodox Statscan is a linear slot scanning X-ray machine. There are two such devices (branded as Lodox Forenscan) operational at forensic pathology laboratories in the Western Cape in South Africa. These devices have been readily adopted where they are installed and are used routinely (Bateman, 2008; Knobel et al., 2000).

Figure 2.1: Scannex system (1994).

Figure 2.2: Early Lodox system (1997).

2.2.1 Lodox history

The Lodox Statscan is a digital X-ray machine that originated as the Scannex, a tool invented by diamond mining company De Beers, which was losing between 10% and 20% of its uncut diamonds to theft by its workers (Vaughan, 2008). The original Scannex system (Figure 2.1) was designed to screen staff to ensure that diamonds were not being stolen whilst exposing the staff to as little dose as possible, and had to comply with international radiation exposure guidelines. The images that the system produced did not only meet the design objectives but also showed great potential for use in medical diagnosis (Boffard et al., 2006; Vaughan, 2008).

This marked the beginning of a biomedical design project; the original clinical prototype (now called Oldox) was installed at Groote Schuur hospital as part of a pilot study in 1996 (Potgieter, 2001; Vaughan, 2008). This device was effectively a horizontal version of the Scannex system (Figure 2.2).

The basic design criterion was to develop a trauma scanner that was diagnostically equivalent to that of the existing film X-ray systems. This Oldox system was foundational in specifying considerations for the design of the first true clinical Lodox Statscan, installed in the trauma department at Groote Schuur Hospital during July 1999. Focus areas were maximising access to the patient for resuscitation and minimising the amount of X-ray exposure of the patient and staff. The system (Figure 2.3) was successful: a full body X-ray could be produced and the patient X-ray dose was reduced by 90%. The image quality was diagnostically equivalent to that of existing analog X-ray machines. An added advantage was a drastic reduction in the time taken to perform a scan (Vaughan, 2008).

2.2.2 Lodox Statscan system specifics

The main reason for the low X-ray dose of the Lodox Statscan system is the slot-scanning feature. A narrow "fan beam" of X-rays is projected through the patient onto a detector. Source and detector are coupled to opposite ends of the c-arm and move together from head to toe as the patient is scanned.

Figure 2.3: True medical prototype (1999).

Multiple rows of the detector are used for each portion of tissue – these values are clocked along the Charged-coupled device (CCD) sensor and are summed incrementally: this improves the signal to noise (S/N) ratio, reducing the required dose. Additionally, having a smaller detector means that the scatter that reaches the detector is significantly lower than that of standard full field radiography. More than 95% of the scatter is removed, eliminating the need for an anti-scatter grid.

The detector used in the Lodox Statscan is a proprietary ultra low noise Time Delay and Integration (TDI) CCD detector, similar to that found in a multidetector computed tomography (MDCT) scanner. The scintillator used in the detector is a Rarex Green Fast intensifying screen.

The Lodox Statscan machine consists of a mechanical part in Figure 1.1 and a control computer in Figure 2.4. The control computer is where patient details are entered and scanning parameters are set.

2.2.3 Lodox Statscan operation

The Lodox Statscan is designed to take several projection images of a patient, normally an anteroposterior view (c-arm positioned as in Figure 1.1) and a lateral view. There is also the option of performing scans at oblique angles (those falling between that of anteroposterior and lateral projections). Patient details need to be entered on the human machine interface (HMI) (Figure 2.4 and Figure 2.5) before a scan can take place. From this same interface patient size and scan procedure are selected. These set the control techniques (X-ray tube settings of mA and KV) which can also selected manually. Also available for user configuration is the detector binning, where the resolution is reduced by the binning number e.g. if 6-pixel binning is selected, a window of 36 of the original image pixels (6×6 pixels) are added together to form a single pixel of the new image. An advantage in using this technique in down-sampling images is that the signal-to-noise ratio of the image is improved.
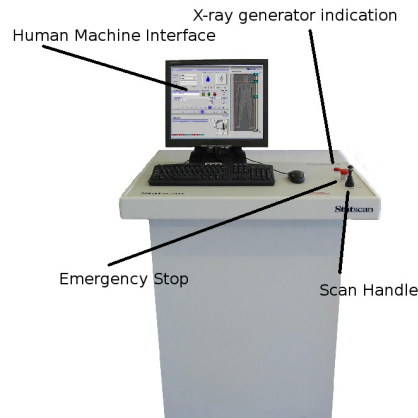
Figure 2.4: Control Computer on the Lodox Statscan.

Actual scanning is done manually by activating the scan handle (Figure 2.4), which acts as a "dead man's switch".

The hardware components that make up the control system of the Lodox Statscan are a Siemens S7-300 range programmable logic controller, which controls the sequence in which actuators such as motors and solenoids on the machine operate whilst monitoring states of sensing hardware. The user interface is in a project running on the Adroit industrial package.

2.2.4 Lodox Statscan X-ray dose

The effective dose of a full body AP scan with the control techniques set at 110kV, 140mA, full speed 140mm/s and a 0.4mm collimator gap is 99uSv, with the entrance dose at 0.12mGy (Irving et al., 2008).

For a conventional thoracic CT image the entrance dose is expected to be in the range of 20mGy to 50mGy (Nickoloff and Alderson, 2001; Israel et al., 2010).

A worst case scenario of all of the Lodox AP scans penetrating the same surface of tissue over a set of 182 scans would have a cumulative X-ray exposure of $182 \times 0.12mGy = 21.8$mGy, which is within the range of a conventional CT scanner for a thoracic CT scan.

2.2.5 Forensic application of Lodox Statscan

Roentgen presented the first human X-ray image, of his wife's left hand, in 1895. In the same year an X-ray examination was first used in a medicolegal case, presented in court to show a bullet that a physician was unable to remove and was still lodged in the patient's leg. In just three years X-ray images were being captured to aid examining a dead body (Poulsen and Simonsen, 2007).
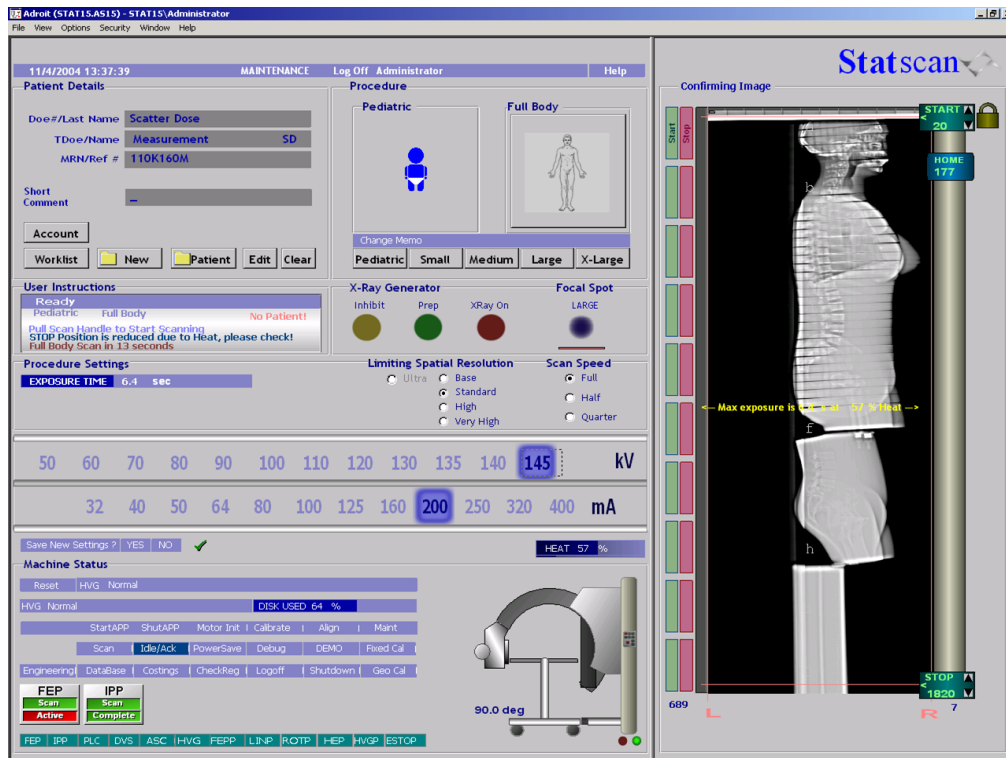
Figure 2.5: The Lodox Human Machine Interface.

Cape Town has been labelled the murder capital of South Africa, with Salt River forensic pathology laboratory performing 15 autopsies a day (Bateman, 2008). About half of the cases are murder and half of those are caused by firearms (Knobel et al., 2000). All of the projectiles need to be retrieved carefully as the rifling is important in ballistic investigations. Without reliable X-ray facilities, finding bullets can be a lengthy process as the bullet may have deflected off of bone and changed direction. Also, bullets lodged deep in bone (such as in the lumbar spine) are almost impossible to locate using dissection alone (Knobel et al., 2000). A Lodox Statscan with adjustments for the tissue density and timing of exposure customised for scanning dead tissue was installed and commissioned at Salt River. This device, dubbed the "Forenscan", was installed in December 2007 (Bateman, 2008).

2.3 Computed tomography

Computed tomography uses X-ray energy to generate 3D information of the anatomy in the form of 2D slices or axial views. The earliest CT scanners made use of a scanning process where a pencil beam source and coupled detector were moved linearly to produce parallel beam projection data. Once data for an angle was complete, the source and detector would be rotated slightly to the next angle and a new projection data set scanned. This scanning procedure would be repeated for the angular range of interest.
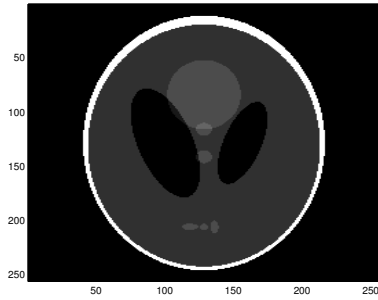
Figure 2.6: The original phantom to be reconstructed.
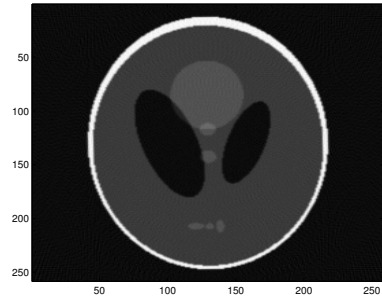
Figure 2.7: Reconstruction performed from 0° to 180°.

ontext group tonight...
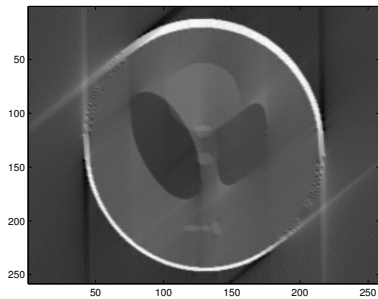
Figure 2.8: Reconstruction performed from 0° to 135°.
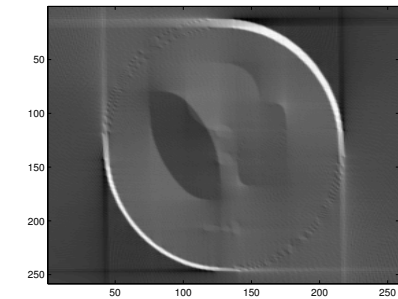
Figure 2.9: Reconstruction performed from 0° to 90°.

For full angle tomographic reconstruction, parallel beam projections are required over at least 180° (Figures 2.6–2.9). For fan beam projections this is normally increased to 180° plus the fan angle (Parker, 1982). The Lodox c-arm angle has range 0° → 90°, so to acquire enough images two sets must be scanned with the trolley rotated in between. Practically, two image sets are acquired from 0° → 90°, one upright and one upside down.

Rotating the upside down images to an upright orientation means that effective scanning has taken place from 0° → 90° and 0° → −90°, which fulfills the reconstruction requirements.

2.3.1 Beer's law

Beer's law describes how X-rays interact with matter, where an object of unit length has the physical tendency to attenuate an X-ray by the attenuation coefficient μ.

An X-ray beam with intensity I_0 incident on a body is attenuated according to the relation,

$$I(x) = I_0 e^{-\mu x}, \tag{2.1}$$

where I is the final X-ray intensity, x is the path length (cm), and and μ is the attenuation coefficient of

the particular material. The attenuation coefficient μ is given in cm^{-1} (Dove, 2001).

For real bodies, the total X-ray attenuation is made up of a sequence of different anatomical structures with different μ values and different lengths,

$$I = I_0 e^{-(\mu_1 x_1 + \mu_2 x_2 + ... + \mu_N x_N)}. \tag{2.2}$$

2.3.2 Line integral

The line integral is the integral of some value of interest along a line. In the case of an X-ray system, Beer's Law is taken as the integral and can be regarded as a good approximation of an X-ray beam interacting with a body that it is travelling through, from 2.2,

$$I = I_0 e^{\int_l \mu ds},$$

$$P_\theta(k\tau) = ln\left(\frac{I_i}{I_0}\right) = \int_l \mu ds, \tag{2.3}$$

where μ varies throughout the body and is replaced with $f(x,y)$(Kak and Slaney, 1999; Epstein, 2008).

It is assumed that the X-ray is monochromatic and travels through the object in a straight line from the source to the detector.

In Figure 2.10 an object is represented by the two-dimensional function $f(x,y)$. A line integral is taken along line parallel to S, rotated by an angle θ from Y. This ray, at $r = r_1$, is attenuated by all of the $f(x,y)$ (inside of the object) through which the ray passes. This attenuation can be quantified by the line integral

$$P_\theta(r_1) = \int_{(\theta, r_1) line} f(x,y) dk, \tag{2.4}$$

where $-\infty < k < \infty$ and $f(x,y)$ is a function that returns the value of μ at (x,y) (Kak and Slaney, 1999).

This integral is represented by a point in the projection in Figure 2.10, which is the projection of the object at the angle θ at $r = r_1$. The simplest type of projection is the parallel beam projection, where the angle θ is kept constant and the value of r is varied to cover the entire body being projected.
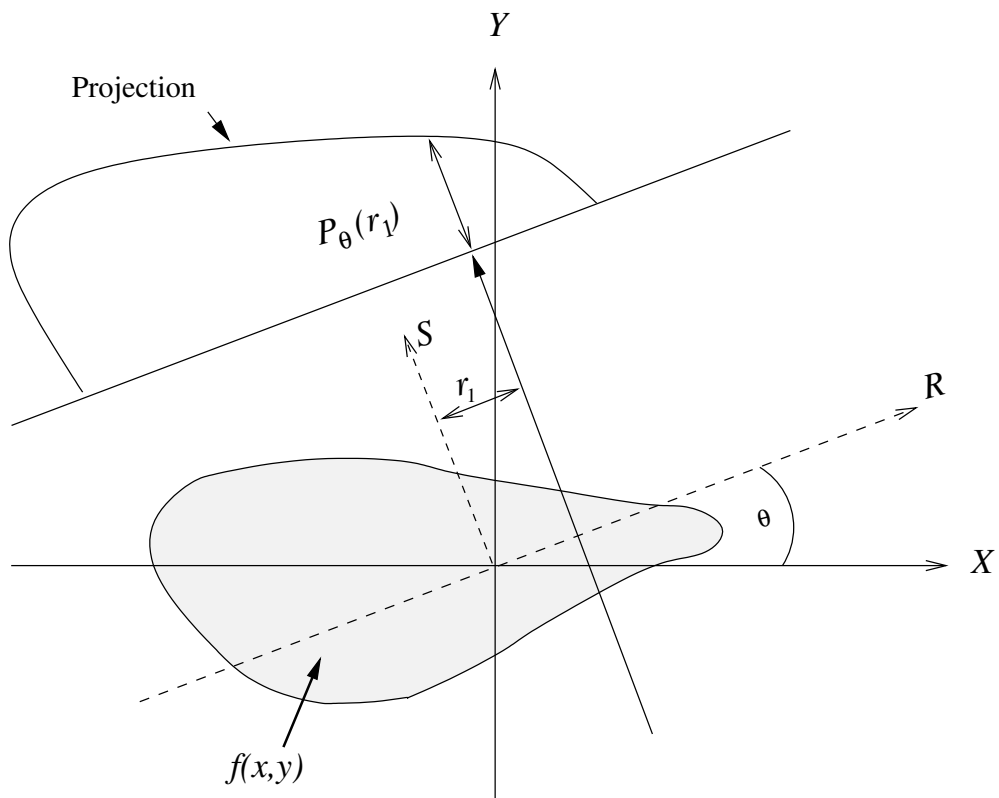
Figure 2.10: Line integral and parallel beam projections.

2.3.3 Radon transform

Using the set of orthogonal co-ordinate axes, R and S, rotated counterclockwise by θ relative to X and Y (Figure 2.10), the transformation between the two systems can be written as

$$\begin{bmatrix} r \\ s \end{bmatrix} = \begin{bmatrix} \cos\theta & \sin\theta \\ -\sin\theta & \cos\theta \end{bmatrix} \begin{bmatrix} x \\ y \end{bmatrix} \quad \text{and} \tag{2.5}$$

$$\begin{bmatrix} x \\ y \end{bmatrix} = \begin{bmatrix} \cos\theta & -\sin\theta \\ \sin\theta & \cos\theta \end{bmatrix} \begin{bmatrix} r \\ s \end{bmatrix}. \tag{2.6}$$

Including a Dirac delta function into the line integral (equation 2.4) gives

$$P_\theta(r) = \int\limits_{-\infty}^{\infty} \int\limits_{-\infty}^{\infty} f(x,y)\delta(x\cos\theta + y\cos\theta - r)dxdy. \tag{2.7}$$

Taking this function over all θ values we can form the function known as the Radon transform,

$$p(\theta, r) = \mathcal{R}(x,y) = \int\limits_{-\infty}^{\infty} \int\limits_{-\infty}^{\infty} f(x,y)\delta(x\cos\theta + y\cos\theta - r)dxdy. \tag{2.8}$$

2.3.4 Fourier reconstruction

To reconstruct the image from the projections, an inverse Radon Transform,

$$f(x,y) = \mathcal{R}^{-1}\left\{p(\theta, r)\right\}, \tag{2.9}$$

is needed.

An alternative is to make use of the Fourier slice theorem, which states that the 1-dimensional Fourier transform of a projection is equal to a slice of the 2-dimensional Fourier transform of the original object (Kak and Slaney, 1999).

The central slice theorem provides a way to achieve a reconstruction: the projections are Fourier transformed and added to the frequency domain. If all of the projections are included into the frequency domain, a 2D inverse Fourier transform can be computed to obtain the image. When a finite number of projections are used, the reconstruction becomes an approximate reconstruction of the image.

2.3.5 Filtered back-projection

Back projection is based on the observation that by smearing the projection over the entire image a rough estimate of the image is obtained. The way that this smearing occurs is that the value of a ray's projection is added to the line perpendicular to the detector direction which is all of the points that the ray passes through (Figure 2.11). Artifacts are introduced due to a finite number of projections being used, and because the rectangular to polar coordinate change causes regions of equal size in rectangular coordinates to be mapped onto regions of different sizes in polar coordinates, depending on the distance from the origin. This is exhibited by the inclusion of the l factor in the transform

$$\Delta x \Delta y = l \Delta \theta \Delta l, \tag{2.10}$$

where a polar coordinate transform is defined as referring to a position using the coordinate pair of distance from the origin (l) and the rotational angle from a reference direction (θ).

Filtered back-projection includes a filter that magnifies the contribution further from the origin. The simplest filter is a limited ramp filter (Figure 2.12). Other filters that can be used include the Shepp-Logan, the Hann and the Hamming filters, which smooth and suppress high frequencies producing better image quality (Dove, 2001).

In the final algorithm, each projection is filtered and then "smeared" across the reconstruction image. The projection is Fourier transformed to the frequency domain before being filtered and is inverse Fourier transformed back to the original space afterwards. Filtering occurs in the frequency domain, with the transformed projection being multiplied by a filter function. After the inverse Fourier transformation, the filtered projection is the contribution to the reconstruction for a single angle. All of the different angular filtered projections are back-projected by being "smeared" across the image at an angle perpendicular to the projection angle.

2.3.6 Three-dimensional reconstruction

Three-dimensional (3D) reconstructions can be formed by stacking multiple two-dimensional reconstructions (Kak and Slaney, 1999). The maximum spatial resolution in the z-axis of $360\mu m$ per slice (3.1.4), where every row in the projection image is reconstructed and stacked together.

A distortion could be introduced by the TDI scanning method used by the Lodox as a small but finite amount of fanning is happening in the z-direction.

The ability to view a set of axial 2D reconstruction images can give the viewer and indication of the 3D volume that has been reconstructed. Three-dimensional rendering techniques are beyond the scope of this thesis.
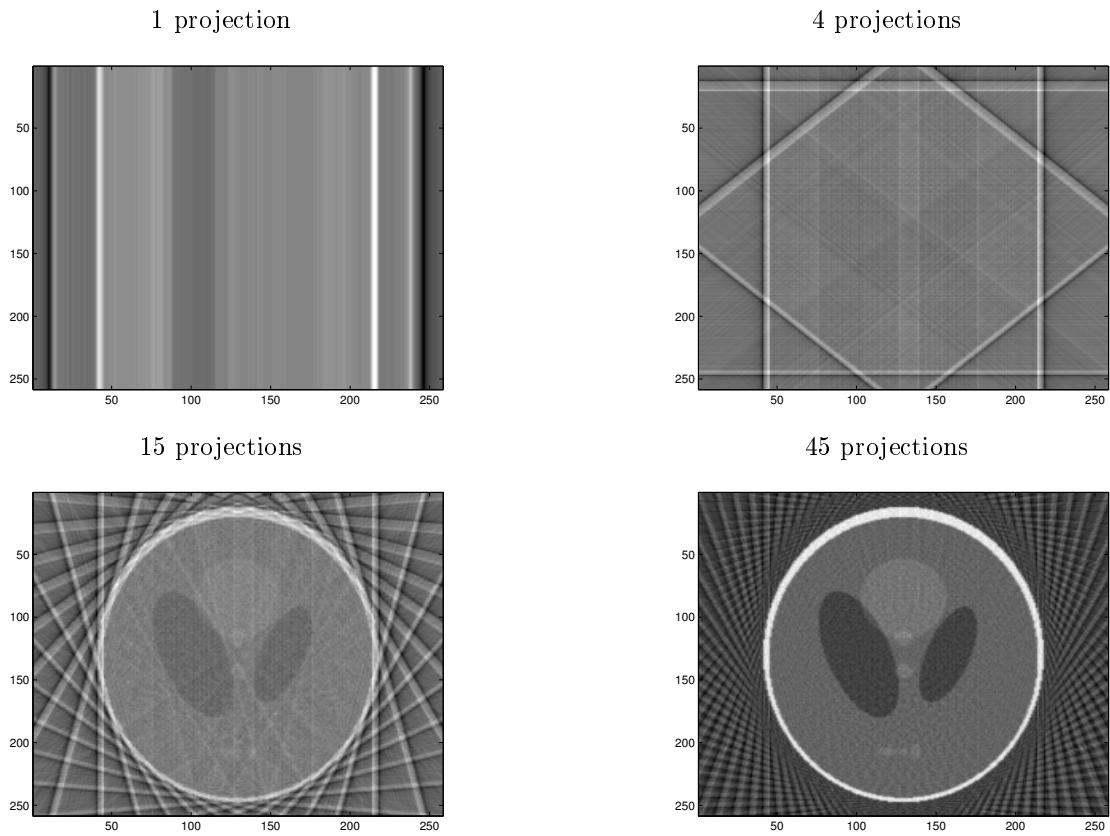
Figure 2.11: Filtered back-projection conceptual drawing.

Figure 2.12: Frequency domain data and the need for a filter (Kak and Slaney, 1999).

2.4 Fan beam reconstruction

Orthogonal beam projection is a slow method of generating CT datasets. A more practical way of generating projection data is to use a fan beam. This is where a homogeneous beam is limited to a cone which passes through a small parallel slot to form a fan-shaped beam. This beam is directed through the object being scanned towards a bank of detectors. The reduction in scan time comes at the cost of increased complexity in the reconstruction (Kak and Slaney, 1999). There are two different fan beam configurations used in computed tomography, which are determined by the configuration of the detectors. These are equiangular rays (Figure 2.13) and equally-spaced collinear detectors (Figure 2.14). The equiangular configuration is where the angle between each sample is the same: detectors placed on a circle have equal spacing and they can be modelled as unequally spaced detectors on a straight line. This is a practical configuration used in commercial CT scanners. Equally-spaced collinear detectors do not have equal angles between the projections, as the detectors are equally spaced on a straight line (Kak and Slaney, 1999).

For both of these, the fan projection beam configuration needs to be compensated for, either by resorting into parallel beam data (Figure 2.15) or by using an adapted filtered back-projection algorithm that takes the specific fan beam geometry into account.

Since the Lodox Statscan most closely resembles an equispaced fan beam configuration, this is what is explored in this thesis. As the Lodox Statscan does not have the ideal equispaced fan beam, a transformation of the Lodox projection data to fan beam data is required. The approach taken is to combine the transform from Lodox geometry to equispaced fan beam geometry and the transform from equispaced fan beam geometry to orthogonal (or parallel) beam geometry into one transform, the output of which is a sinogram that can be reconstructed using the filtered back-projection method. Re-binning to a parallel beam projection for reconstruction was selected as a readily available and trustworthy filtered-back-projection implementation is available (MATLAB's *iradon* function), the orthogonal beam sinogram data can be used to help develop and verify the calibration functionality and the use of discrete blocks could allow easier division of the software into subsystems for later development.

2.4.1 General fan beam reconstruction (projective model)

In Figure 2.16, define the world coordinate system as a left-handed coordinate system with the positive y-axis pointing downwards and with the origin at the c-arm's centre of rotation.

Point P is a sample projection point defined to have the vector position p in the world coordinate system (X,Y). The same point can be referenced by different vectors defined in different coordinate frames. This same point is at p'' in the coordinate system (X'', Y''), which is a rotated form of the world coordinate system. The same point is also at p' in the camera coordinate system (X', Y'), a coordinate system that is a translated form of the system (X'', Y''). The coordinate transform from p to p'' is a matrix rotation

$$p'' = R_\theta p, \tag{2.11}$$
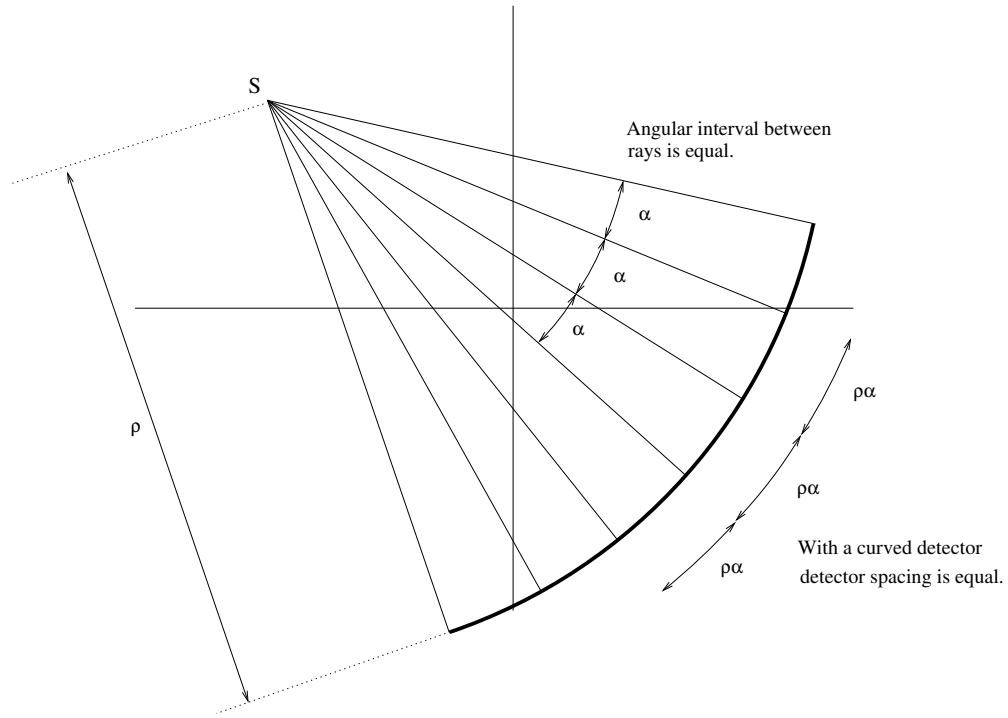
Figure 2.13: Equiangular fan beam.
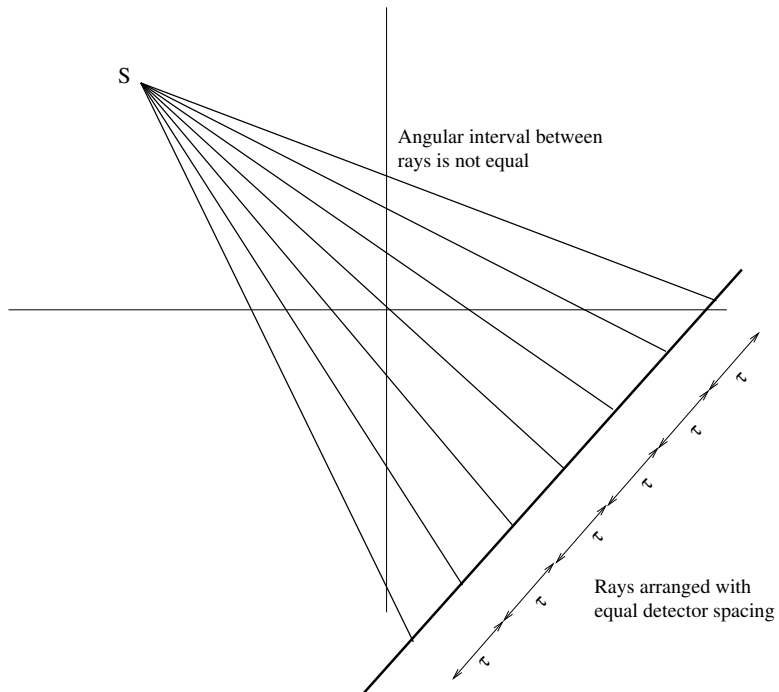
Figure 2.14: Equispaced fan beam.
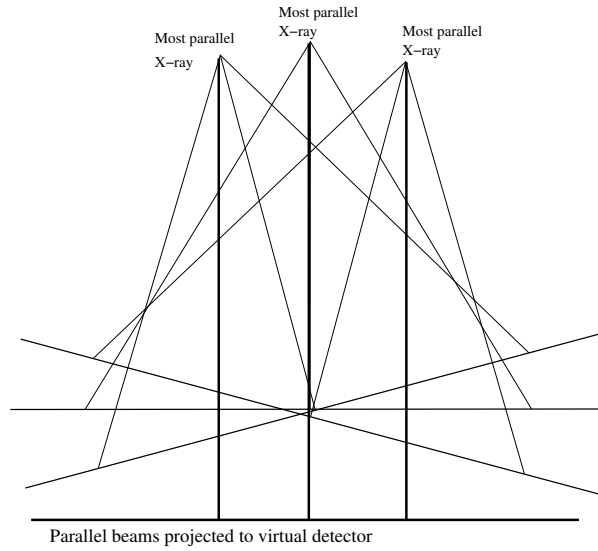
Figure 2.15: Fan beam resorting.

where R_θ is the rotation matrix of the c-arm,

$$R_\theta = \begin{pmatrix} \cos\theta & -\sin\theta \\ \sin\theta & \cos\theta \end{pmatrix}. \tag{2.12}$$

The coordinate transformation from p'' to p' is a translation

$$p' = p'' + p_r', \tag{2.13}$$

where p_r' is the translation matrix of the coordinate system origin:

$$p_r' = \begin{pmatrix} dr \\ dh \end{pmatrix}. \tag{2.14}$$

Combining these transformations gives a transform from p to p',

$$p' = R_\theta p + p_r'. \tag{2.15}$$

The projection of the point P at (X', Y') onto the detector is

$$x = d\frac{X'}{Y'}. \tag{2.16}$$

All of the transforms that have been performed up to now make use of position coordinates in millimetres (mm), with x as the position measure on the detector. This detector is a camera with pixels as the unit of measure ρ. A transform from x to ρ is

$$\rho = \frac{x}{a} + \rho_0, \tag{2.17}$$
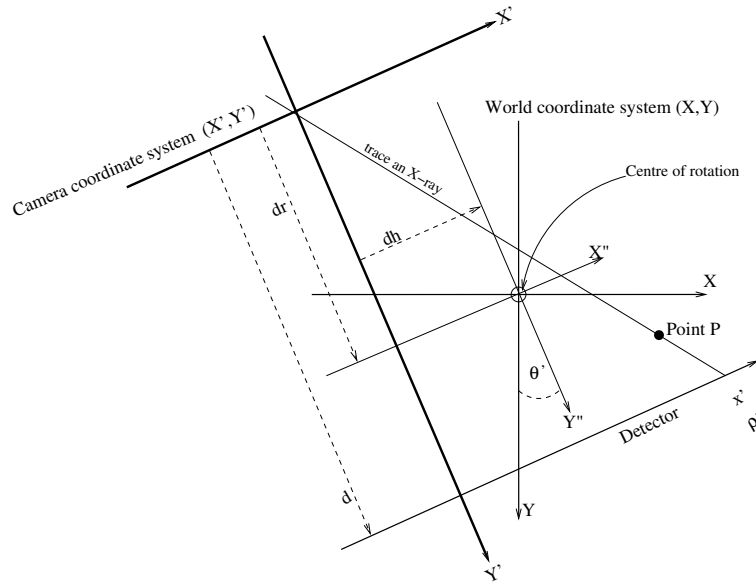
Figure 2.16: General fan beam projection and coordinate system transformations.

where a is the pixel size and ρ_0 is the pixel corresponding to $x = 0$ (this is the detector element to which the principal ray would project, and where Y' and the detector coincide).

2.4.2 Estimating parameters for fan beam tomography

The geometry of the Lodox Statscan can be described as a general fan beam configuration. In order to perform filtered back projections on data generated using the Lodox Statscan, the geometric transformations in Section 2.4.1 need to be performed on the image data to produce an equivalent parallel beam dataset. The geometric transformations require X-ray system dimensions (the source-detector distance d, the source to centre of rotation distance dr and the centre of rotation-principal ray distance dh), the detector parameters (the pixel size a and the pixel to which the principal ray projects ρ_0) and, for each projection, the c-arm angle. The free parameters in the geometric calibration are d, dr, dh, and the c-arm angles θ_1 to θ_N, with the detector parameters a and ρ_0 fixed.

In (de Villiers, 2000), the c-arm angles are manually measured with a digital spirit level and, although no explicit mention is made of how the geometric measures are acquired, it would appear that the measurements were made using a tape measure or steel rule.

In (de Villiers, 2004), conventional methods of measuring the distances were identified as not being practically possible, as the centre of rotation is a virtual point (the c-arm does not rotate about a single bearing on an axis) and because the actual location of the source is inside the tube and is therefore inaccessible for measurement. A computational method was used to calculate the dimensions from the projections of a calibration object. This calibration object consisted of a perspex board with a regular grid of 9 pins, each with different length. The cross-sectional spatial coordinates are known *a priori,*

using 36 pin-to-pin measurements and an optimisation process. Projections of these pins are present on all scans, the pins are manually identified on each of the projections, and the geometric values and c-arm angles are solved for using a local search algorithm that minimises the least-squares reprojection error.

2.5 Modern tomographic technology

Although the scope of this project ends with producing a method to generate filtered back projection images, studying the state-of-the-art tomography topics shows the direction in which the research and the commercial market is moving. Tomosynthesis is an imaging procedure is used largely for mammography, tomosynthesis should be possible using Lodox images, although an application has not been identified. Sparse angle tomography should also be possible but does provide much value in medical imaging and is more suited to industrial imaging.

2.5.1 Tomosynthesis

Tomosynthesis is an image reconstruction technique where a set of projection scans over a narrow angular range is used to generate longitudinal slices, and the procedure based on linear-scan tomography (Grant, 1972). The shift-and-add tomosynthesis technique reconstructs the plane of tissue that coincides with the fulcrum of the source-detector pair that move parallel to one another. The use of a c-arm mechanism requires a special technique called isocentric motion where the isocentric projection is reprojected onto a virtual planar detector (Dobbins and Godfrey, 2003).

Isocentric motion tomosynthesis should be possible with the Lodox Statscan. Tomosynthesis is an active field with mammography applications being investigated extensively (Fang et al., 2010; Teertstra et al., 2010), as well as the science involved in more general applications of tomosynthesis (Kanaka et al., 2010).

2.5.2 Sparse angle tomography

Filtered back projection requires X-ray penetration from all the way around the object being scanned at a high angular resolution, but often mechanical limitations prevent this from happening. Sparse angle tomography is the science of producing reconstruction images from a dataset generated with a low angular resolution. The under-sampled sinograms in sparse angle tomography are analogous to "pixellated photographs" and the reconstructions produces images from which the centre of mass and a mass distribution can be identified, whereas the region boundaries are difficult to identify. Sparse angle tomography useful for industrial imaging but not very applicable to medical imaging (Constantino and Ozanyan, 2008).

The measuring lengths and positions of hard radio-opaque regions in the body (e.g. projectiles and knife blades) could prove to be a useful forensic application of sparse angle tomography using the Lodox.

2.6   Geometric calibration phantoms

Literature exists demonstrating that calibration of c-arm X-ray systems has been explored before.

(Mitschke and Navab, 2003) presents geometric calibration of a c-arm system different to the Lodox, but with similar challenges and constraints. A calibration phantom with radio-opaque markers is used, which needs to be visible in each of the images. A projection matrix is used to estimate the geometry from a set of projected markers. These calibration markers are not practical to be included in the actual patient scanned data, so either a CCD camera which is mounted to the X-ray tube or an external navigation system is used to generate this transform from optical data.

(Cho et al., 2005) employs a calibration frame with 24 steel ball bearings in 2 plane parallel circles. The projection of the the two circles of markers to ellipses is used to determine the position and orientation of the X-ray system relative to the calibration frame coordinate system. Both of these X-ray calibration methods are performed on cone beam c-arm machines and are not performed at the same time as patient data is scanned, but rather to characterise the c-arm trajectory or an optical camera system.

Chapter 3

System Design

Producing tomographic reconstructions using the filtered back projection algorithm requires orthogonal beam projection data. Functions are developed to generate a set of orthogonal beam projections from Lodox Statscan images by generating important geometric parameters using markers embedded in the imaging space.

The order of the sections follows the procedure one might adopt in generating tomographic reconstructions using the Lodox Statscan. Firstly, the X-ray machine is set up and a set of images are produced. The images are then exported from the Lodox Statscan and sent to an image processing workstation where an image processing procedure corrects for the variable image start position. Custom hardware (included in the scanned images) and software estimate the Lodox Statscan geometric parameters required to generate an orthogonal beam projection data set from a Lodox Statscan data set. Finally tomographic reconstruction is performed, producing axial slice views from the orthogonal projection data.

3.1   Scanning procedure

Manual scanning of an image set for tomographic reconstruction using a Lodox Statscan is costly in terms of the time taken to scan (device time and operator time), and is costly for the X-ray machine as it places some strain on the X-ray tube and generator.

Problems with the AMI Lodox Statscan (the device at the University of Cape Town, made available for this thesis investigation) caused significant project delays, and when the system was again operational intermittent scanning failures plagued the scanning process. The AMI Lodox Statscan has subsequently undergone significant upgrades.

This section contains the Lodox Statscan set-up where the actual X-ray imaging parameters used are described, including the X-ray dose parameters (Section 3.1.1). The set of imaging phantom objects to be

scanned is listed and a motivation for each item's selection made (Section 3.1.2). The scanning procedure is described and a process flow diagram is presented (Section 3.1.3). The section concludes with detailing all of the assumptions that were made (Section 3.1.4).

3.1.1 Lodox Statscan set-up

This section assumes some expertise in performing X-ray scanning with the Lodox Statscan. On the control computer (Figure 2.5) a new patient ID is generated and the "Full Body AP" image procedure is selected. The control technique factors are set to 100kV and 100mA, full scan speed, large focal spot and standard resolution (detector binning of 6×6 pixel). The image width should be fully open and a test image should have a 1912px width.

Control technique factors of 100kV and 100mA are typical settings on the Lodox Statscan, and have been used previously for tomographic reconstruction (de Villiers, 2004). The scan speed was set to "full speed" as this option allowed for quick scanning. The large focal spot is system default value and standard resolution was selected to give the best image quality whilst keeping the dataset within a reasonable size (less than 4GB).

The scanning range is set to start approximately $40mm$ after the start of the trolley. This is to allow the c-arm to be moved back and forth without any chance of bumping the trolley and moving the objects being scanned. The scan range is set to stop just after the end of the last object of interest, so that the amount of time that the X-ray source operates is minimized.

The trolley height is set such that the hydraulic cylinder that lifts the table-top is $700mm$ long, so that the detector can be rotated through its entire angular range without colliding with the scan table. Figures 3.1–3.4 illustrate the table in this position, and the the c-arm is able to move freely.

3.1.2 Phantom collection

Calibration objects are required to find the parameters listed in Sections 2.4.1 and 2.4.2. Section 3.3 describes the detailed design of a calibration object. Since $2 \times 90°$ scan sets are required, two calibration objects are included in the scan space, one of which configured for the $0° \rightarrow 90°$ scan set and the other configured for the $0° \rightarrow -90°$ scan set. These are placed at the top of the scan table.

The Lodox Statscan images need to be registered in the scanning direction before they are useful for tomographic reconstruction. Section 3.3 describes decisions made regarding the markers and the method used to perform this registration. The registration markers are two ball bearings placed just below the calibration markers on the table.

Since tomography is often used for measuring object lengths in three dimensions by stacking the slices up to form a volume, a tool to measure spatial accuracy is included. The device is included in Figures 3.5 and 3.6.

Figure 3.1: C-arm at 0°(anteroposterior).

Figure 3.2: C-arm at 30°.

Figure 3.3: C-arm at 60°.

Figure 3.4: C-arm at 90°(lateral).
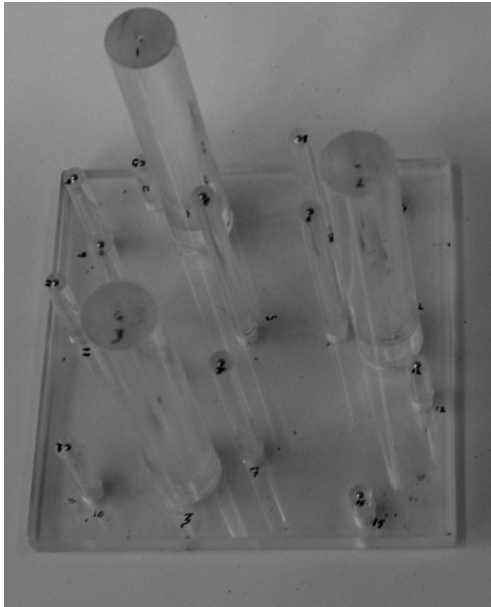
Figure 3.5: Spatial accuracy test phantom.
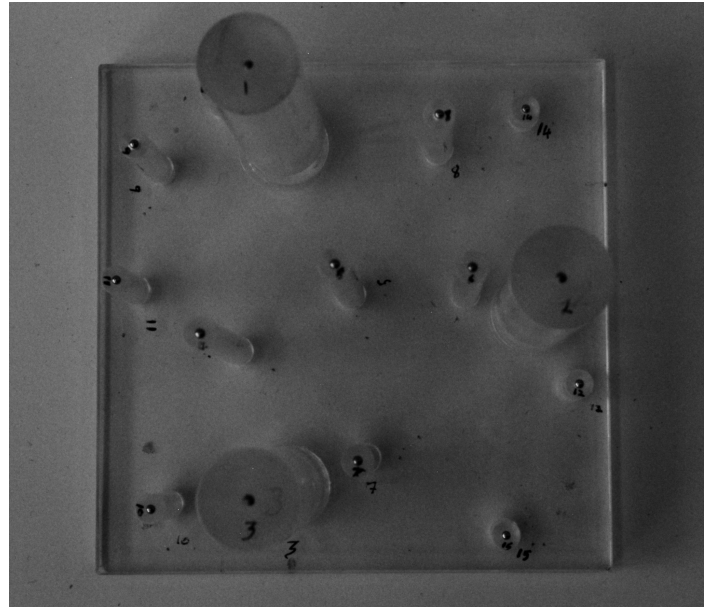
Figure 3.6: Spatial accuracy test phantom.

The Rando Phantom is a tissue equivalent medical imaging phantom made by the Phantom Laboratory in New York, USA. It consists of a human skeleton encased in resin that is radiologically similar to human flesh, and is normally used for X-ray dose measurement. The head section of a Rando Phantom is included in the image set (Figure 3.7 and 3.8).

The Catphan CT phantom is an imaging phantom made by the Phantom Laboratory in New York, USA. It is primarily used for quality assurance testing of CT scanners. It consists of slices of different material and can be used for an assortment of tests (Figure 3.9 and 3.10).

In summary, the objects included in the phantom collection are two calibration objects, two top-of-image markers, the spatial accuracy test phantom, the Rando head phantom and the Catphan CT phantom.

3.1.3   Scanning

The scanning process, shown as a flow chart in Figure 3.11, is performed to generate an image set for tomographic reconstruction.

The scanning is performed at a very high duty cycle for the Lodox Statscan, and although there are heat load interlocks in the system, Lodox Systems recommended that the user pays attention to the heat load of the system and that cool-down breaks be included. The generator heat load can be monitored using the "X-ray tube temperature healthy?" indicator on the control computer (Figure 3.11).

Figure 3.7: Rando phantom head section, photograph.
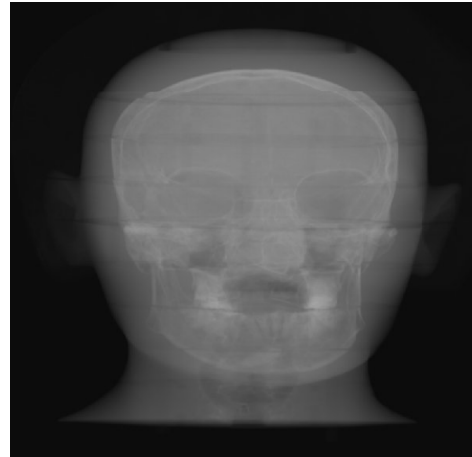
Figure 3.8: Rando phantom head section, AP X-ray image.
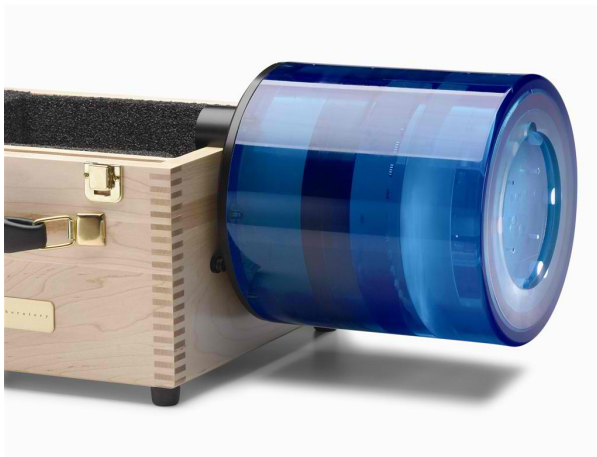
Figure 3.9: Catphan CT phantom photograph.
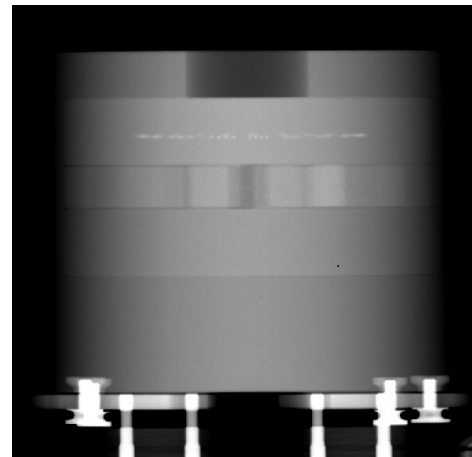
Figure 3.10: Catphan CT phantom photograph, AP X-ray image.
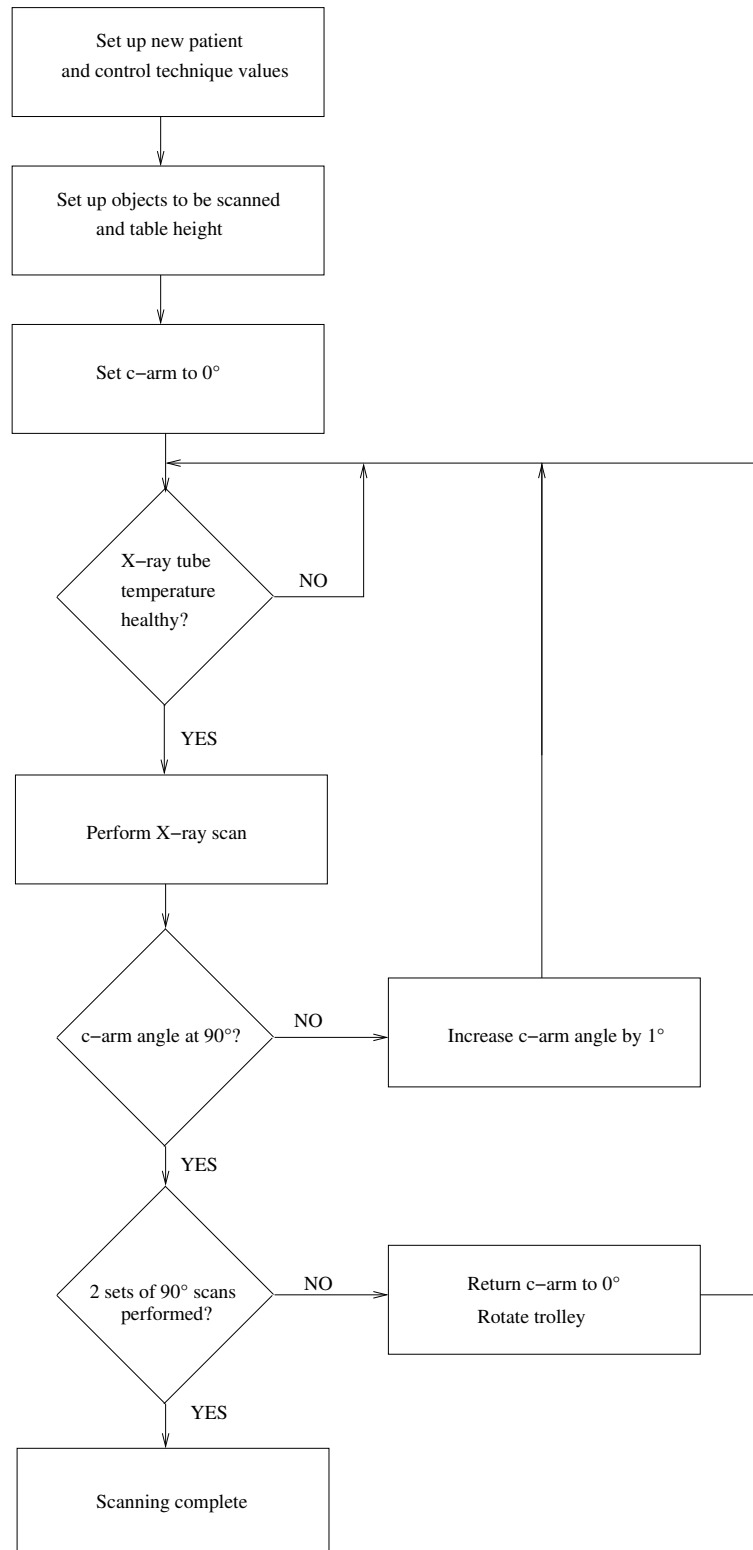
Figure 3.11: Flow chart of the scanning procedure.

3.1.4   Assumptions

The c-arm geometry (d, dr and dh in Figure 2.16) are assumed to be constant for at least the duration of scanning a tomographic reconstruction data set.

The calibration object, the phantom body and the trolley are regarded as a rigid body. Effort was also made to ensure that the trolley remains stationary with respect to the rest of the Lodox Statscan for the duration of the scan.

The pixel size is a function of the optical components in the detector, and of the binning rate used in the scan. The actual detector has a pixel size of $26\mu m$. The fibre optic tapers, which allow the cameras to image a continuous line, have an input size of $61.2mm$ and an output size of $26.77mm$.

A binning rate of 6 pixels is used for tomographic reconstruction. Thus the pixel size in each image will be

$$a = 26 \times 10^{-6} \times \left(\frac{61.2}{26.77} \right) \times 6 = 360\mu m. \tag{3.1}$$

This pixel size is based on datasheets documenting the components used in the manufacture of the Lodox Statscan and are considered reliable.

The subject and the calibration hardware (on the trolley) will be rotated by exactly 180° about the y-axis between the $0° \rightarrow 90°$ and $0° \rightarrow -90°$ scan sets. This means that when the upside-down images in the $0° \rightarrow -90°$ scan set are each rotated by 180°, they are equivalent to the calibration and reconstruction procedure as the images scanned in the $0° \rightarrow 90°$ scan set. A body that is not rotated by an angle other than 180° is equivalent to a movement part way though the scan procedure and the current calibration design will fail to register this movement.

3.2   Moving images from Lodox database to MATLAB

The Lodox Statscan stores X-ray images in a proprietary database, not compatible with MATLAB. A C++ program was written, making use of an API supplied by Lodox that allows access to the image database. On running the application, a graphical interface starts from which a patient, a study and an image can be selected. All of the images for the patient and study selected are exported to DICOM format files, which can be opened with MATLAB (with the image processing toolbox). Each file name is comprised of the patient first name, the patient last name, and the image ID in the database (as a unique identifier).

3.3 Top of image alignment

Tomographic reconstruction algorithms generate a reconstruction of a slice from the projections of that slice. In a conventional CT scanner, guaranteeing the correspondence between the physical tissue slice and the projection data is not a problem since the all of the projections for a slice are acquired before the scanning hardware advances to scan the next slice (newer machines operate with a helical scan and interpolation of the projection data).

The Lodox Statscan data is acquired in the form of full-body X-ray projection images, one X-ray image per projection angle. A sinogram is constructed by selecting a particular image row from each image, this requires that the images are all aligned in the scanning direction. As mentioned in Section 1.4, the control system in the Lodox Statscan is unable to produce images where there is reliable correspondence between the row of the image and the slice of the object being scanned, this was observed on both the AMI Lodox Statscan and the Lodox Statscan at Salt River forensic pathology laboratory.

In order to correct for the variable start positions of the image data, a method is used where a marker is placed on the table, and the image is translated in the scanning direction such that all of the markers fall on the same image row. This effectively registers the images in the scanning direction. The markers are found using image processing techniques.

Discrete markers were chosen over a cross correlation approach as the projection shape over variable c-arm angles is predictable. The projection of the other objects being scanned can vary depending on the c-arm angle, the anteroposterior view (Figure 3.1) and the lateral view (Figure 3.4) being the extreme cases.

This section begins with a description of the top-of-image problem (Section 3.3.1), followed by the design of the hardware part of the solution (Section 3.3.2) and the software part of the solution (Section 3.3.3).

3.3.1 Problem

The Lodox Statscan is unable to produce images that start at a reliable position in the scanning direction (Section 1.5.1) but the images in the data set need to be registered in this direction (the +z direction in Figure 1.1) for tomographic reconstruction to be done. The technique used in this study to perform this registration is to crop the top edge of each image so that a top-of-image marker projects to the same row. To acquire this "top of image" row index, a radio-opaque marker is placed in an otherwise empty region of the X-ray image, and image processing is used to automatically extract the marker location from each image.

Registration of these images is complicated by each X-ray image being scanned at a different c-arm angle (Figure 3.1–3.4). Also, since a set of X-rays is obtained from $0° \rightarrow 90°$ and from $0° \rightarrow -90°$ (after the trolley is rotated), the image registration marker must be identifiable in both scan sets.

3.3.2 Hardware solution

A spherical calibration marker was selected as the projection of a sphere is the same from all viewing points (projecting to a circle in a cone-beam configuration and to an ellipse in the Lodox configuration). The specific markers used are ball bearings as they are clearly distinguishable in X-ray images (a high contrast marker allows for simple thresholding), they are highly-accurately manufactured (trustworthy spherical shape) and they are available at low cost. The marker needs to be placed in an otherwise empty region of the image, with a large enough empty space on either side (in the scanning direction, z-axis) such that the marker will be found in all scans.

A marker diameter of $8mm$ diameter was chosen as this size ball bearing is readily available. It is a convenient size as it is small enough to not take up much room in the image, yet is large enough to give adequate contrast against the table.

During preliminary scanning it was found that scans performed near the lateral angle (those with c-arm angles from 80° to 90°) have X-rays projected along the width of the bed and are heavily attenuated by the table top (Figure 3.12). In the X-ray images the contrast between the marker and the projection through a large section of table top is not high and the two regions overlap, making the marker difficult to distinguish automatically from the surroundings (Figure 3.13).

Through experimenting with the marker position on the bed it was found that moving the marker to near the right hand edge of the bed means that the projection of the marker does not overlap the distinct region of the projection of the bed, and the marker is identifiable in all of the images.

Placing a marker on the right hand side is only useful for one scan set with a $0° \rightarrow 90°$ range (Section 3.3). The trolley is rotated before the second scan set is performed. A logical solution is to place a second marker near the left edge of the bed (on the right edge after rotating trolley) to register the set with a $0° \rightarrow -90°$ range. An example scan with the two markers included is presented in Figure 3.14.

3.3.3 Software solution

In the first scan set, the marker on the right-hand side of Figure 3.14 is the top-of-image marker. The position of the marker is manually read off of the AP image (the first image scanned); the row index of the marker's position forms the middle of a horizontal search window that spans 50 rows above and 50 rows below it (the window bounded by the horizontal lines in Figure 3.14). This search window spans the entire width of the image and should contain nothing other than the marker and the scan table. A threshold function with a hard-coded threshold is applied to this region.

In the foreground region (projection image values above the threshold) there will either be the projection of just the marker (Figure 3.15) or the projection of the marker and part of the table surface (Figure 3.16) as well as some small noise artifacts. The projection of the spherical markers with Lodox Statscan is an ellipse due to the magnification that occurs in the fan beam but not in the scanning direction–analogous to a line source (Forsyth and Ponce, 2002) or a push-broom camera (Hartley and Zisserman, 2003).
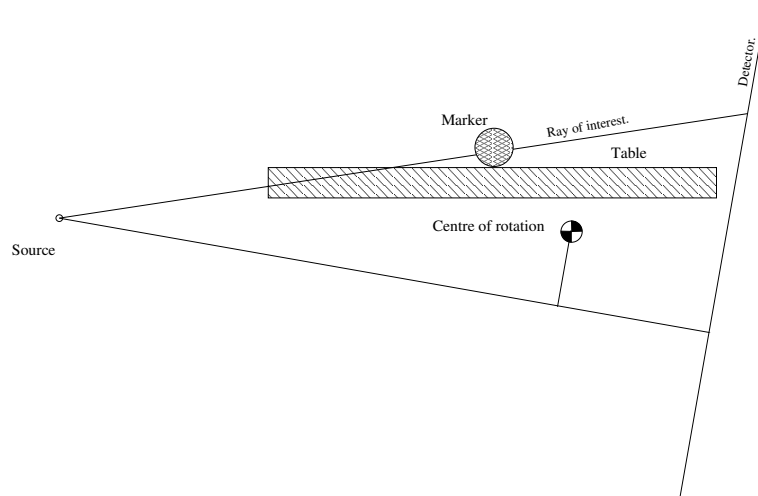
Figure 3.12: Marker occluded at high scanning angles.

Figure 3.13: X-ray of occluded marker.

Fortunately the elliptical projection of the marker is the most round of all of the large items that the threshold function generates. A minimum size of object that is considered a candidate for the marker is an area of 100 pixels, and this is used to remove noise artifacts present in the image.

To find the projection of a spherical marker, a roundness metric

$$rm = 4\pi \left(\frac{area}{perimeter^2} \right) \tag{3.2}$$

is applied to all of the foreground regions with an area of more than 100 pixels. The foreground region found to be most "round" is the region having the largest rm value and this is identified as the projection of the marker. Once this region is found, its centroid is easily recovered. The row index of the centroid is the start row index and the image can be cropped accordingly.

The images of the second set are rotated upright, and the process used on the first set is repeated for the second scan set. For this set of images the marker on the left-hand side of Figure 3.14 is used.

These two scan sets are then aligned to each other using the right-hand marker present in the first image (anteroposterior view) of each scan set.
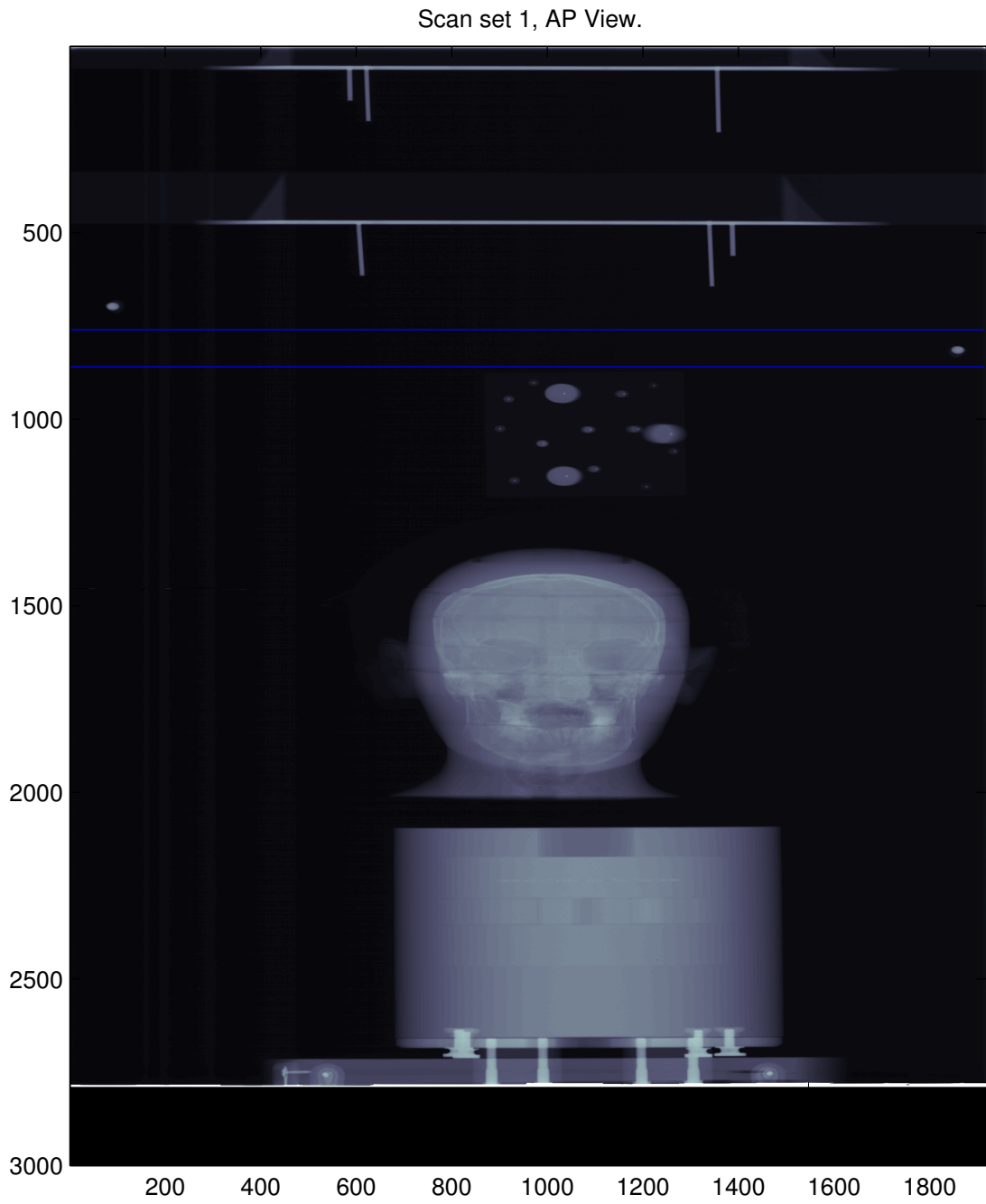
Figure 3.14: Lodox projection image.
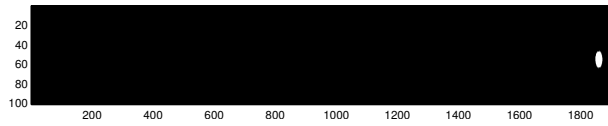
Figure 3.15: Threshold image with only the marker present.
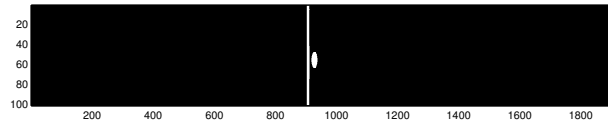
Figure 3.16: Threshold image with marker and table artifact present.

3.4 System geometry and c-arm angles

From the general fan beam projection calculations (Section 2.4.1) it is known that several geometric parameters and the c-arm angles of the projections are required in order to reproject images from the general fan beam geometry to orthogonal beam projection geometry. From Section 2.4.2 it is known that these geometric measures are not practically measurable. The c-arm angle at which an X-ray image is acquired is displayed (at scan time) on the Lodox Statscan control computer, but this value is not saved as meta-data in the image database and may in any case not be accurate. These two sets of measures may be generated using information in the projection data.

A set of calibration markers are included in each of the X-ray projection images. These are radio-opaque metal pins pointing in the scanning direction and mounted rigidly to form a calibration object, which needs to be included at the same physical location in space and projected in each image of a scan set. The design of the calibration object includes selecting the number of markers and their geometric configuration, as well as the material to use and the associated structure keeping them rigid in a calibration tool.

In each X-ray image the calibration object is projected onto the image, and image processing is performed on a relevant region to extract the marker projection positions on the detector.

A mathematical model of a general fan beam geometry system is formulated, including the same number of calibration markers present in the actual projection data and the same number of projection angles as is used in the actual image set. A set of virtual projections is generated using the mathematical model and the format of these results needs to correspond to the output of the image processing performed on the real projection data.

A cost function is defined to be the difference between the real projection positions and the simulated projection positions. A set of system geometry and c-arm values matching the real system should produce a zero error, and values that are not representative of the real system should produce a high cost. A non-linear least squares optimisation of the cost is performed to generate a set of geometric values that describe the real system.

Performing this system approximation using the projections of both scan sets ($0° \rightarrow 90°$ and $0° \rightarrow -90°$) at once poses a problem. Previously it was found that it was necessary to rotate the object being scanned about the principal ray in order to combine the two scan sets to form a $-90° \rightarrow 90°$ set (de Villiers, 2004). Not knowing where the principal ray is, and trying to get objects centred along the line makes this difficult to do exactly in a practical system. One way to overcome this problem is to perform two separate partial reconstructions, one for the $0° \rightarrow -90°$ set and one for the $0° \rightarrow 90°$ set. Translation of the trolley between the scan sets will affect the position of the trolley in the reconstruction, and is corrected by translating the $0° \rightarrow -90°$ reconstruction before summing it with the $0° \rightarrow 90°$ reconstruction. The amount by which to translate the reconstruction can be found by manually annotating at the pixel indices of the $0° \rightarrow 90°$ and $0° \rightarrow -90°$ reconstructed calibration marker slices, or can also be automated.

Sections 3.4.1 and 3.4.2 details with the design of the physical calibration object, Section 3.4.3 describes with modelling the calibration object. In Section 3.4.4 the image processing performed is described and Section 3.4.5 contains a formulation of the cost function used to approximate the system.

3.4.1 Calibration markers

The design of the calibration marker set consists of selecting how many markers are required and their geometric configuration. A larger number of markers should produce a better approximation of the system configuration but also complicates the image processing required to extract the marker locations. In this project it was considered desirable to keep the image processing as simple and as robust as possible by using the minimum number of markers required by the geometric model and cost function.

To determine the minimum number of calibration markers needed, assume K markers are present in the calibration object. Each projection will generate K projections and with N c-arm angles we have KN equations with $4 + 2K + N$ free parameters (where there are N c-arm angles, K x-coordinate values and K y-coordinate values for the marker position and 4 geometric measurements that characterise the Lodox Statscan geometry). If

$$KN \geqslant 4 + 2K + N, \tag{3.3}$$

(e.g. for $K = 2$ and $M = 8$ or $K = 3$ and $M = 5$) then the system is overdetermined and can be solved.

In practice, three markers is found to be smallest practical number. This is because with just two markers the effect of translation and rotation get bundled together (Figures 3.17 and 3.18), whereas with three markers the variables of translation and rotation are distinct and get encoded to their positions (Figures 3.19 and 3.20).

As the three markers are scanned over a c-arm angle range of $0°$ to $90°$ the position on the detector to which each marker projects will change, but correspondence of the physical marker order to the projected marker order is required. If the order in which the projection of calibration markers change or the projections occlude one another, this complicates matters in designing an automated process to identify the marker locations. Placing the markers in an L-shaped configuration should allow the markers to be scanned over a $90°$ range with marker 1 always projecting to the leftmost position, marker 2 to the middle
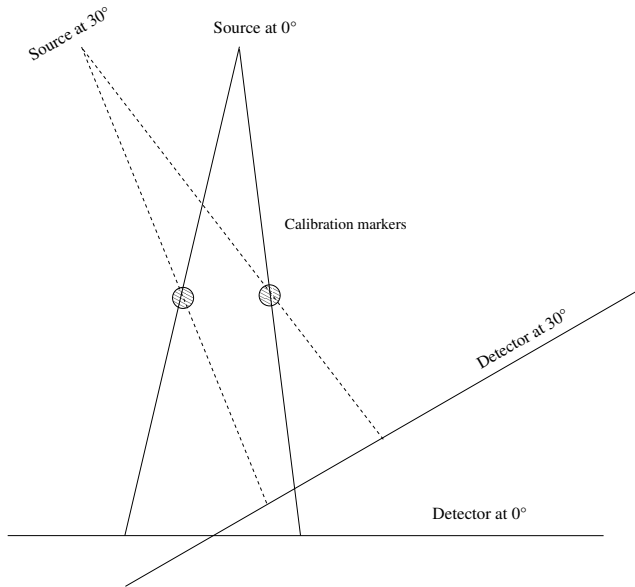
Figure 3.17: Two markers, θ changed between the two cases.
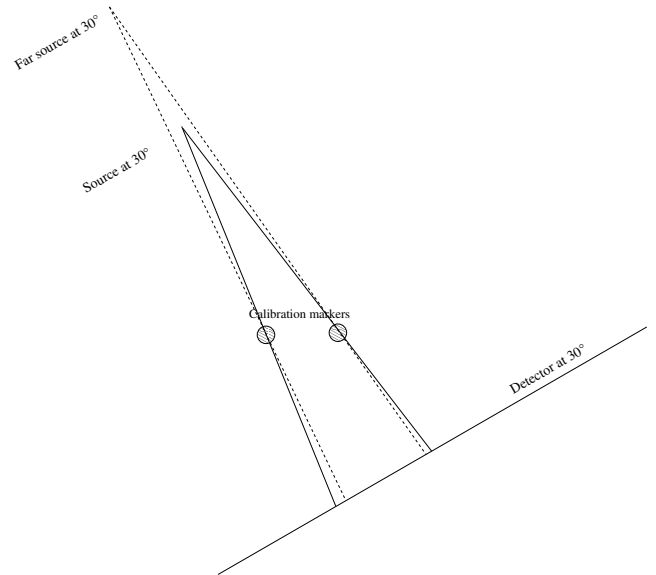
Figure 3.18: Two markers, r changed between the two cases.
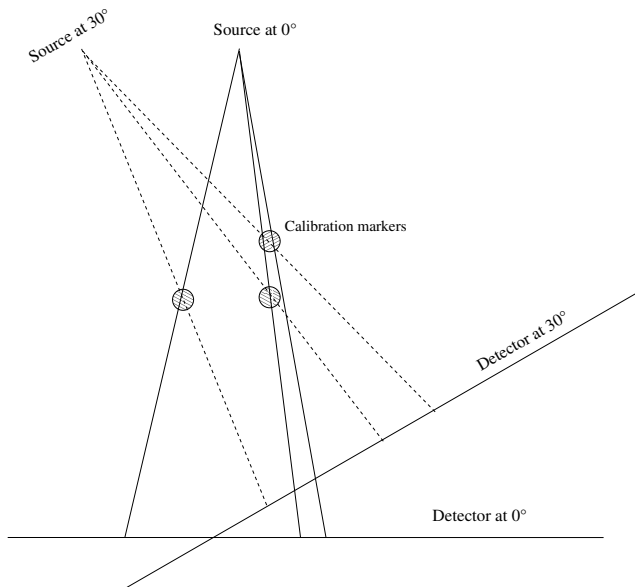
Figure 3.19: Three markers, θ changed between the two cases.
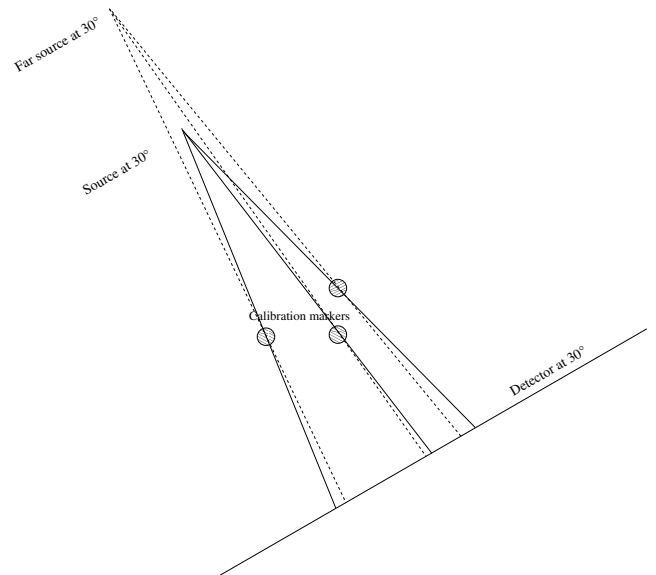
Figure 3.20: Three markers, d changed between the two cases.
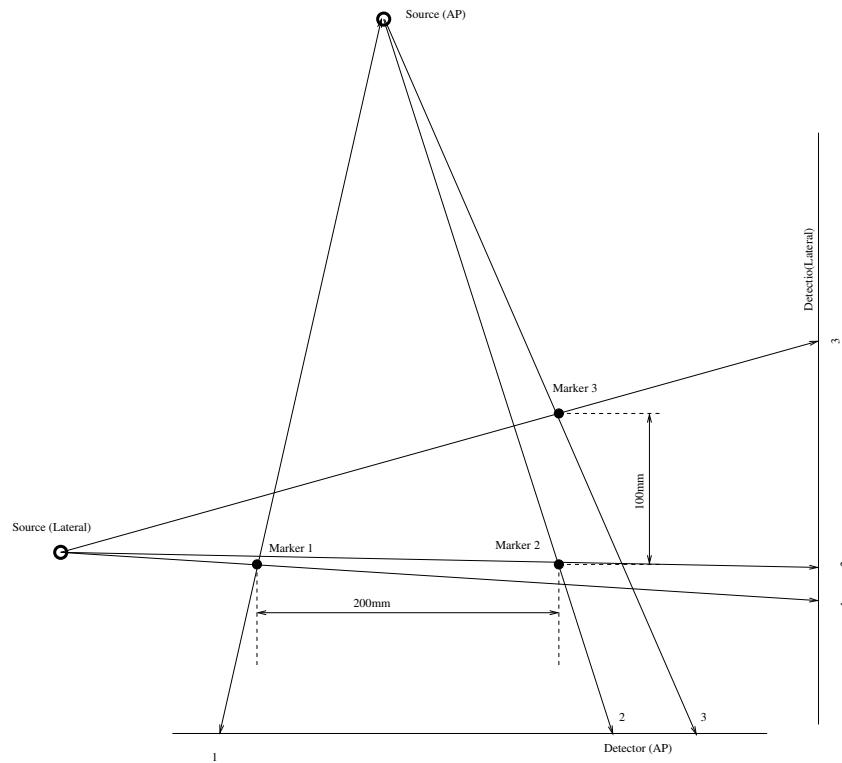
Figure 3.21: Pin locations and simulated projection.

position, and marker 3 to the rightmost position on the detector (Figure 3.21).

A row of the image containing the projected markers is taken and a threshold function is applied, which should yield three positive intervals representing the three projected calibration markers. The middle of each positive interval is the column index of the calibration marker projection (Figure 3.22 and 3.23).

3.4.2 Calibration marker tool–practical implementation

The calibration markers used are $3mm$ brass pins that have been "press fit" mounted into a $300mm \times 300mm \times 3mm$ perspex board. This board is finger jointed to a $700mm \times 50mm \times 10mm$ perspex base. There is a $3mm$ thick perspex fillet to help keep the joint rigid and at $90°$ (Figure 3.24). Brass was chosen for the marker pins as it a metal (radio-opaque) and is easy to acquire and to machine. The tool was designed in a CAD package and laser cut, so the hole placement accuracy as well as the right angle between the base and the board is reliable. As the calibration marker tool was made as a configurable platform where the number and position of markers could be varied, a 3×3 equally-spaced hole pattern is present . The design was based on (de Villiers, 2004), which used a similar configuration. The hardware included in the scans is shown in Figure 3.25.

Although the positions of the holes in the calibration frame are known to be accurate, rotational orienta-
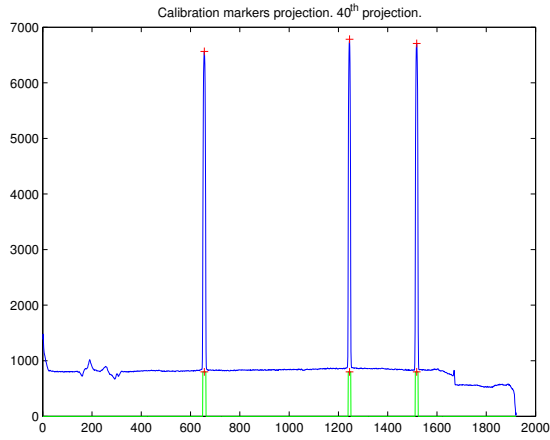
Figure 3.22: Plot of projection of pins, threshold output and pin medians.
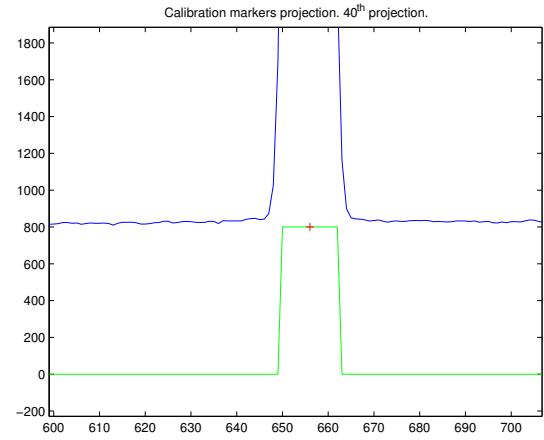
Figure 3.23: Close-up view of a pin projection, threshold and the pin median.

tion of the calibration object on the scanning table (about the y-axis in Figure 1.3) cannot be controlled perfectly. The position of the markers will thus be considered variable in the modelled system.

3.4.3 Lodox Statscan software model

The image pixel size (a) is fixed and constant at $a = 360\mu m$ (for 6×6 pixel binning). The rest of the geometric parameters (Figure 2.16) will be varied and are considered free parameters to be estimated in the geometric calibration. These are:

- source-detector distance (d),

- source-centre of rotation distance (dr),

- principal ray to centre of rotation (dh),

- distance from the leftmost point of the detector to where the principal ray strikes (X_0),

- 2D coordinates (X_a, Y_a) for each of the K markers in the calibration object in the world coordinate system (the left-handed coordinate system origin at the centre of rotation and the +y axis pointing vertically downwards), and

- c-arm angle for each of the projections in a scan set ($\theta_1, \theta_2, ..., \theta_N$).

Using the coordinate system transforms presented in Section 2.4.1 allows the projections of the model's calibration marker points to be calculated for any given set of parameters. The set of markers have the
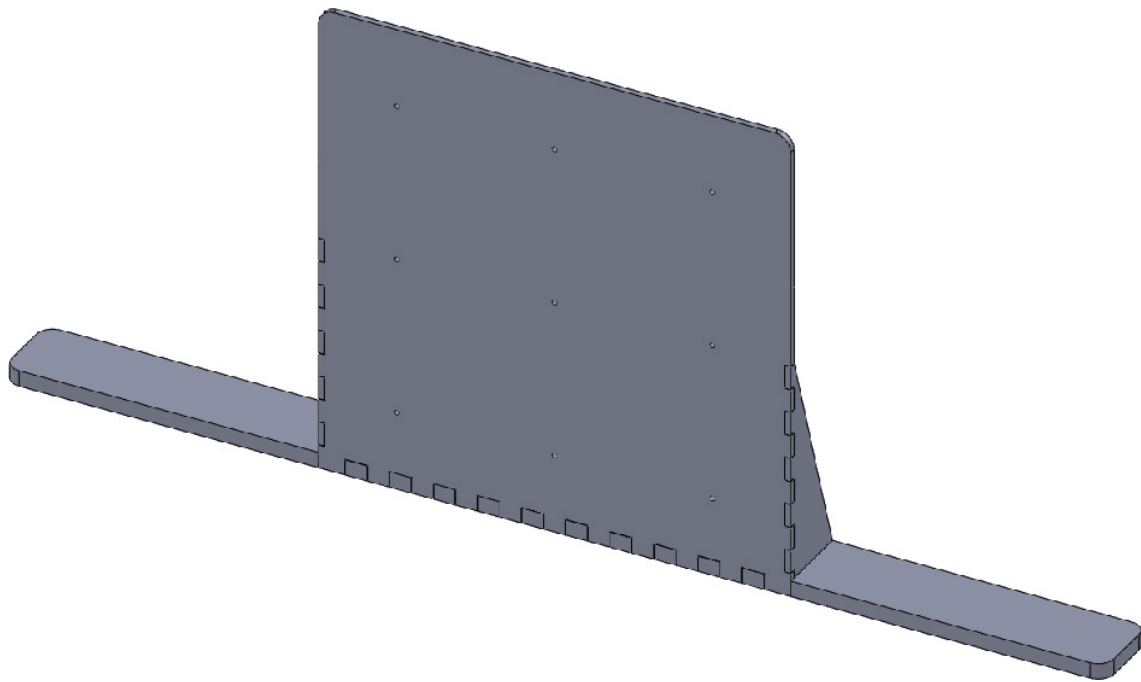
Figure 3.24: Design view of calibration marker frame.
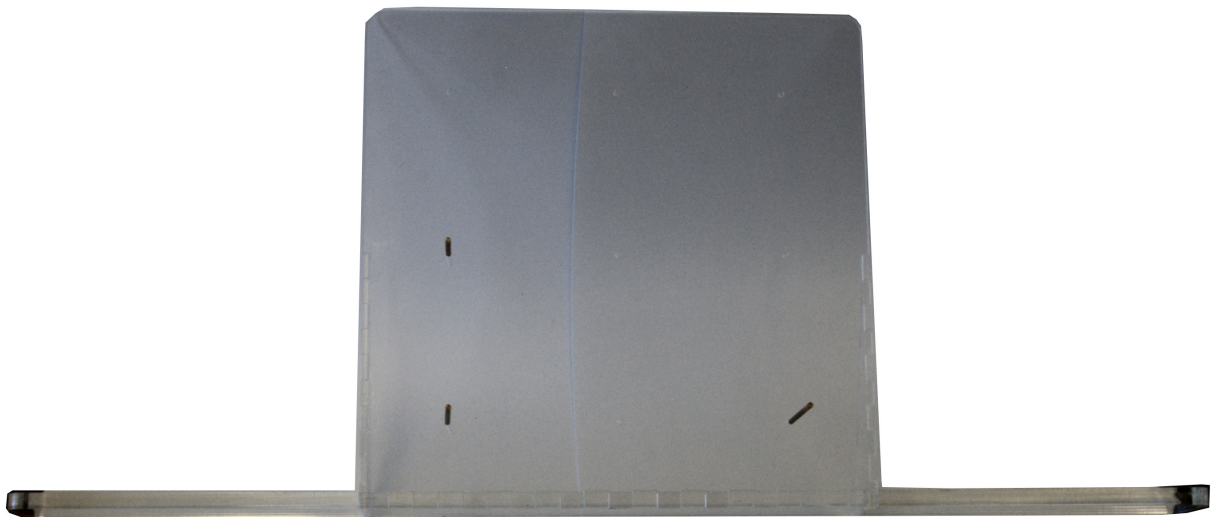
Figure 3.25: Photograph of calibration marker frame.

coordinates in the world coordinate system

$$\text{Markers} = \begin{bmatrix} X_1 & X_2 \ldots & X_K \\ Y_1 & Y_2 \ldots & Y_K \end{bmatrix}. \tag{3.4}$$

The transform from the world coordinate system to the camera coordinate system consists of a rotation by θ (the c-arm angle) and a translation (from the centre of rotation to the source), producing points in the camera coordinate system (with origin at the X-ray source and the +y axis pointing along a line perpendicular to the detector):

$$\begin{bmatrix} X_1' & X_2' & \ldots X_K' \\ Y_1' & X_2' & \ldots Y_K' \end{bmatrix} = \begin{bmatrix} \cos\theta & -\sin\theta \\ \sin\theta & \cos\theta \end{bmatrix} \begin{bmatrix} X_1 & X_2 \ldots & X_K \\ Y_1 & Y_2 \ldots & Y_K \end{bmatrix} + \begin{bmatrix} dh \\ dr \end{bmatrix}. \tag{3.5}$$

The projection (in mm) of the i_{th} marker is $x_i = \left(d \times \frac{X_i'}{Y_i'} \right)$.

The i_{th} marker projects to the pixel $p_i = \frac{(x_i + X_0)}{a}$ in the virtual detector.

Performing the projection for the K markers of one image set produces the projections $\begin{bmatrix} p_1, p_2 & \ldots & p_K \end{bmatrix}$.

For all of the c-arm values of a scan set $(\theta_1, ..., \theta_N)$ the virtual projections are arranged in a convenient matrix:

$$P_{simulated} = \begin{bmatrix} p_{(1,1)} & \cdots & p_{(1,K)} \\ \vdots & \ddots & \vdots \\ p_{(N,1)} & \cdots & p_{(N,K)} \end{bmatrix}. \tag{3.6}$$

3.4.4 Identifying the calibration markers in image data

In Section 3.3 all of the projection images are registered in the scanning direction.

As the calibration markers are pins pointing in the scanning direction, there are multiple rows in which their projected position can be identified. A threshold function is applied to an arbitrarily chosen row containing all three of the calibration markers. Both the row index and the threshold level are hard-coded. The output of the threshold function is a binary vector with a length that is equal to the X-ray image width, and it should contain exactly three foreground regions each representing the projection of a calibration marker.

The middle of each of these three regions is identified as the column index of the projected calibration marker. These three column indices are copied into a matrix with three columns (one for each calibration marker) and N rows (one for each of the N X-ray images), and the result is an $N \times 3$ matrix of marker projections, called P_{image}.

3.4.5   Cost function to model the Lodox Statscan

The Levenberg-Marquardt method of optimisation has been used previously for a similar problem involving estimating a device geometry from projection data (Gullberg et al., 1987). This optimisation method cannot handle underdetermined systems (Mathworks, 2009), which means that the the system needs as many equations as the number of degrees of freedom. The number of projected points represents the number of equations and the degrees of freedom are the set of variables to optimise (the geometric parameters and the c-arm angles). Optimisation of the variables

$$x = \{\theta_1,\, \theta_2,\, \ldots,\, \theta_N,\, d, dr, dh,\, X_0 \text{ and markers } (X_1, Y_1, X_2, Y_2, \ldots, X_k, Y_k)\},$$

subject to the values that are considered constant, $P_{measured}$ (a set of values generated using image data) and a (a value assumed true, based on the dimensions in the camera assembly) by minimizing the cost function $\sum |f(x)|$, where $f(x)$ is the matrix

$$f(x) = P_{measured} - P_{simulated}(x). \tag{3.7}$$

The optimisation uses the MATLAB optimisation toolkit function *lsqnonlin* (Mathworks (2009)), which is a readily available implementation of the Levenberg-Marquardt function.

3.5   Image reconstruction

Producing axial slice views from Lodox projection data is presented in this section. A partial reconstruction approach is used whereby each 90° projection set is kept separate whilst in the projected form (X-ray projection images, Lodox sinogram and sinogram) and then merged once the filtered back projection is performed. This approach is motivated in Section 3.5.1.

Projection data from actual X-ray images is used to compose Lodox sinograms in Section 3.5.2. The difference between the Lodox sinograms and orthogonal projection sinograms is also described.

The Lodox sinograms are transformed into sinograms in Section 3.5.3, which are used to form partial reconstructions and then full reconstructions in Section 3.5.5.

3.5.1   Motivation for the use of the limited-angle reconstruction method

Between scanning the first data set ($0° \rightarrow 90°$) and the second data set ($0° \rightarrow -90°$), the table is rotated 180° about the y-axis (Figure 1.3). Although care is taken to position the trolley close to the original position after the rotation, a two-dimensional translation is introduced (this can be observed in image data: values from an example image pair are illustrated in Figure 3.26.) Registration is performed in the z-direction (Section 3.3). Correcting for a translation in the x-direction in the projection data is not practical; each image is produced with a different c-arm angle and a translation in the x-direction would
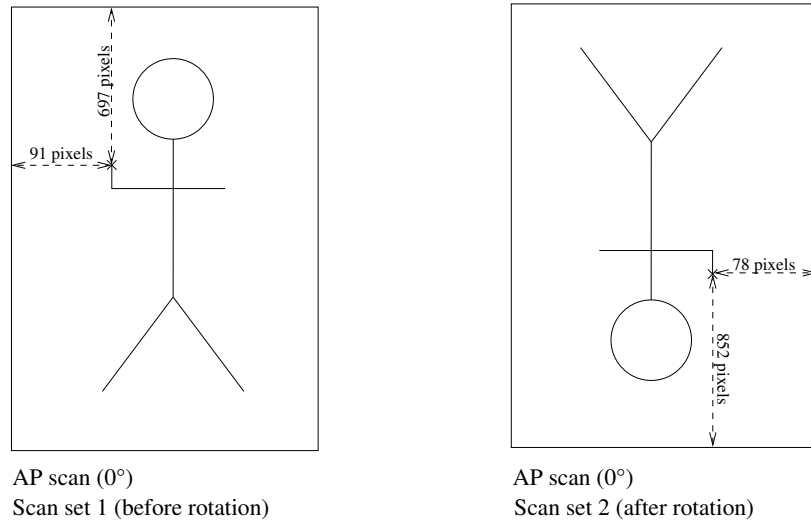
Figure 3.26: Example of the translation introduced when rotating the trolley.

introduce a scaling and a translation of an object's projection, which is impractical to reverse.

Instead, a limited angle tomographic reconstruction is performed for the two scan sets, producing two partial reconstructions per slice. A cross correlation is performed in a region of the image where discrete points are easily identifiable (e.g. the region containing the calibration markers) to find the translation between the two sets. Reversing this translation on one of the sets registers the two limited angle reconstructions.

The two registered limited angle reconstruction sets are then summed (added pixel by pixel), producing an effective reconstruction of the full scan set $(-90° \rightarrow 90°)$.

The limited angle reconstruction procedure for an example phantom image is presented in Figure 3.27.

3.5.2   Lodox sinograms

In Section 3.4.3 the process for acquiring Lodox geometric values and c-arm angles is described. These are used by the coordinate transform function (Section 2.4.1) to generate an orthogonal beam projection set from the Lodox projection data. A MATLAB function to perform the transformation was supplied by Fred Nicolls and is documented in (Nicolls, 2010).

For each of the images in the scan set, the image row that is to be reconstructed is copied to a column of a new array, called a Lodox sinogram. The Lodox sinogram has a height equal to the number of columns of the source image and width equal to the number of projections of the object. The two Lodox sinograms for each image row have dimensions 1921×91 pixels.

The Lodox sinogram is different from a sinogram because there is a distortion introduced by the Lodox
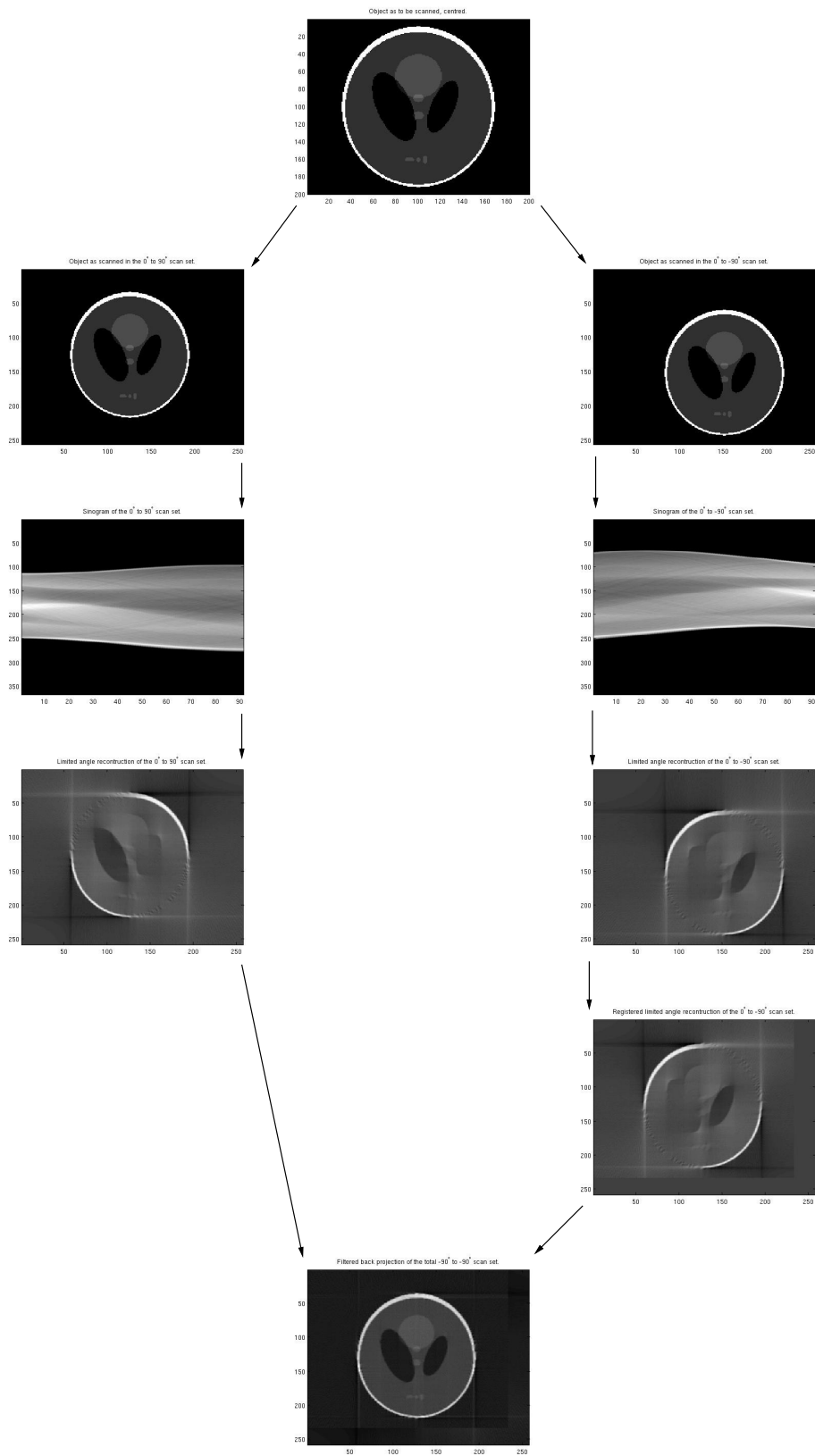
Figure 3.27: Workflow of the limited angle reconstruction procedure.
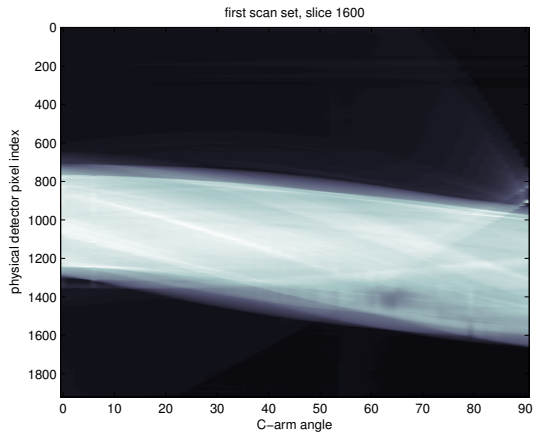
Figure 3.28: Lodox Sinogram example (first set, Rando head phantom).
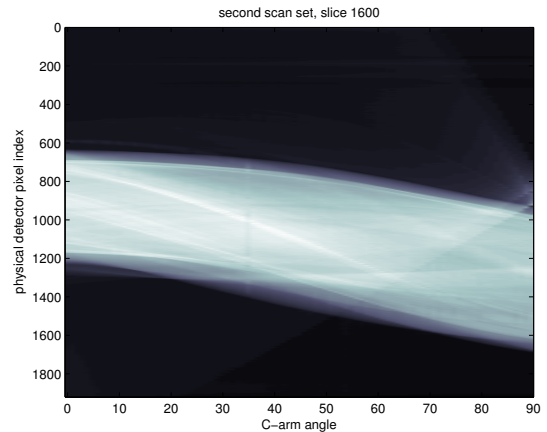
Figure 3.29: Lodox Sinogram example (second set, Rando head phantom).

Statscan having a "general" geometry.

Example Lodox Sinograms are included in Figures 3.28 and 3.29.

3.5.3   Lodox sinogram to sinogram transformation

Two actions are required to transform a Lodox sinogram to a sinogram: a transformation of projection data from the Lodox general fan beam geometry to orthogonal beam projection data, and a rebinning to a convenient size for reconstruction. Both of these actions are performed in a single process.

It is necessary to specify the desired sinogram size, which can be determined from the desired reconstruction image dimensions. The reconstructions in this work are 512×512 pixels at a resolution of $1mm/$pixel. Working from a reconstruction slice of 512×512 pixels, the sinogram height would be equal to the maximum length an orthogonal beam projection through this square would produce, which is the diagonal across the square slice image (Figure 3.30 (Mathworks, 2008)). This has a length $\sqrt{512^2 + 512^2}$ = 724, which means that a sinogram height of 724 pixels is required. Indexing this sinogram such that the zero row is at the middle produces the rows (-362$\leq$row$\leq$361). The angular resolution of the sinogram is selected to match that of the scanned data (i.e. 1°).

The angular range of the sinogram is chosen to be larger than that of the c-arm range such that it holds all of the reprojected Lodox sinogram data. A sinogram with an angular range of $-20° \rightarrow 120°$ is chosen to be at least large enough to hold the result of transforming a $0° \rightarrow 90°$ Lodox projection set. The output sinogram size is determined by transforming a test matrix the same size as a Lodox sinogram (1920×91 pixels), consisting of ones, to an orthogonal projection set using approximate Lodox geometry and adjusting the size of the output sinogram to hold the entire result. The resultant sinograms are shown in Figure 3.31 and 3.32.
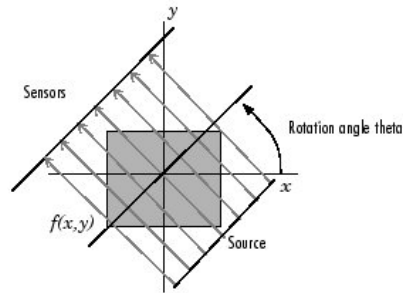
Figure 3.30: Orthogonal projection at 45°(Mathworks, 2008).
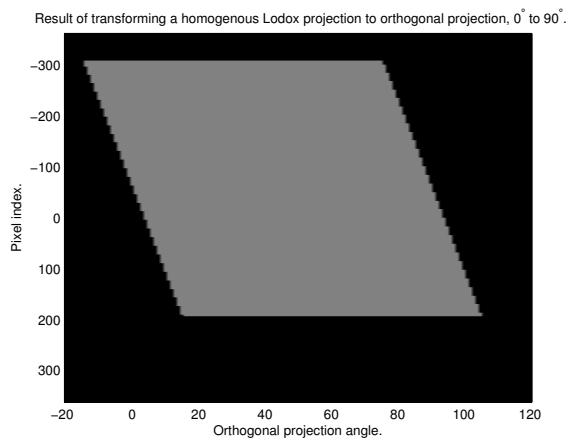
Figure 3.31: Test of the Lodox to orthogonal transforms for the first scan set.
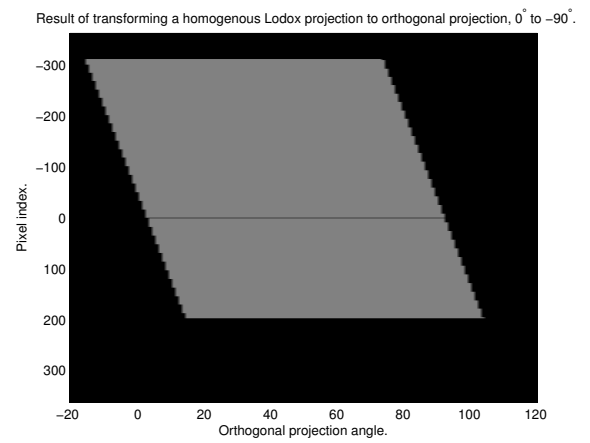
Figure 3.32: Output of the Lodox to orthogonal transform for the second scan set.
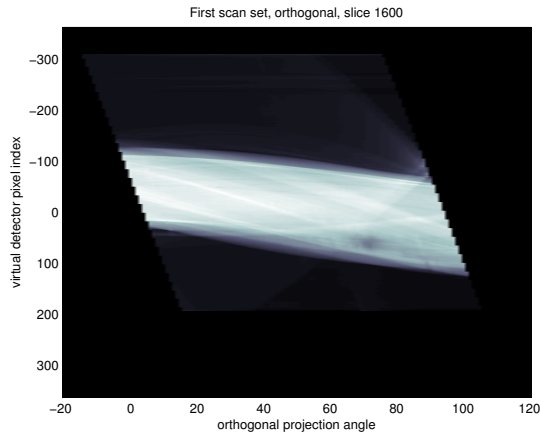
Figure 3.33: Sinogram reprojection (first set, Rando head section).
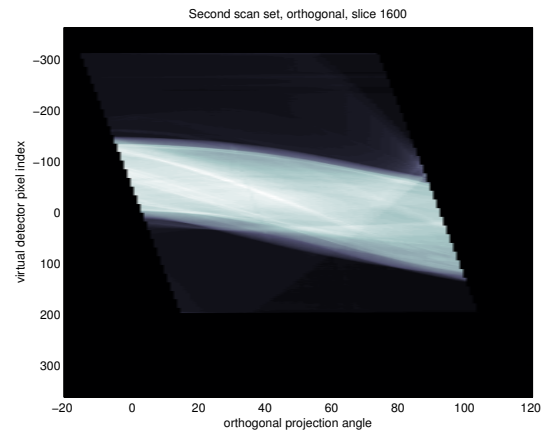
Figure 3.34: Sinogram reprojection (second set, Rando head section).

Performing the Lodox sinogram to sinogram transformation on projection data in Figures 3.28 and 3.29 produces the sinograms in Figures 3.33 and 3.34.

3.5.4 Sinogram angular range

The large angular range for the sinogram of $-20° \rightarrow 120°$ in Section 3.5.3 was chosen to hold all of the projection data. The impact of this large angular range with sheared sinogram edges is explored here. The sinogram in Figure 3.35 has vertical lines drawn to indicate the different angular ranges that are reconstructed. Figures 3.36–3.39 contain the filtered back-projections over these angular ranges. A trade-off is introduced between a desire to have artifact-free images (which requires a reduction in angular range to remove the sheared sinogram edge) and a desire produce a true reconstruction (in which each element in the slice is projected at every angle over a 180° range, requiring all of the available sinogram data). To produce a good reconstruction, the sinogram region is manually adjusted to suit the object being reconstructed.

3.5.5 Limited angle reconstructions

The image reconstruction steps described in Sections 3.5.1–3.5.4 are combined and examples of the images at different stages are found, generating a reconstruction of the Rando head phantom. The slice to be reconstructed is shown in Figures 3.40 and 3.41. Lodox sinograms are produced for the row of interest for the first and second scan sets (Figures 3.42 and 3.43), which are transformed to orthogonal sinograms (Figures 3.44 and 3.45). Including only the columns that contain full projection reduces the width of the orthogonal sinogram (Figures 3.46 and 3.47).
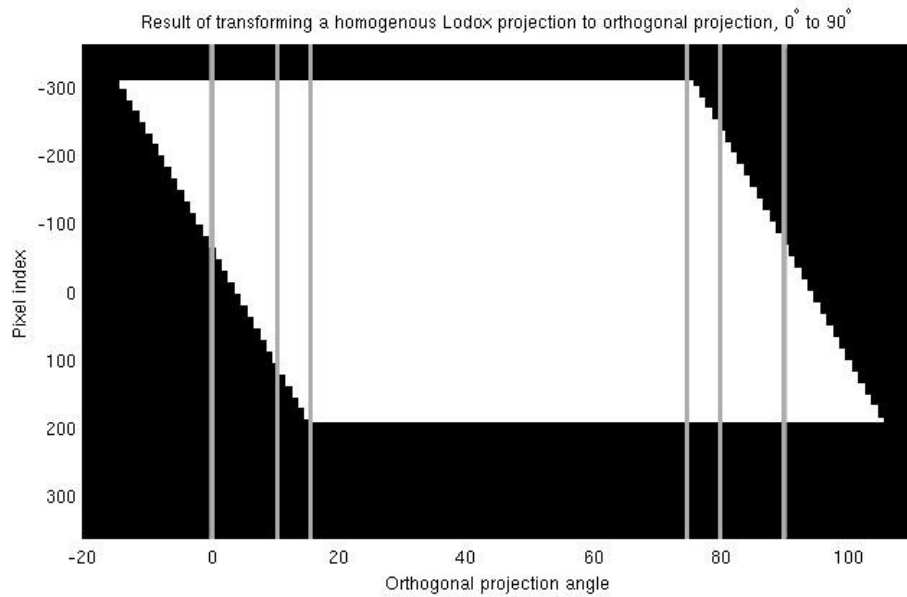
Figure 3.35: Lodox to orthogonal transform of homogeneous test data, with lines included to indicate angular ranges.

Filtered back projection is performed on Figures 3.46 and 3.47 to produce limited angle reconstructions (Figures 3.48 and 3.49).

Correlating the two limited angle reconstructions to register them and adding the aligned images produces a tomographic reconstruction (Figure 3.50).
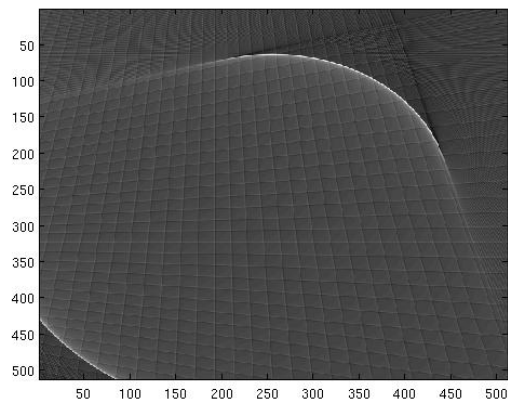
Figure 3.36: Limited angle reconstruction performed from $-20° \rightarrow 120°$.
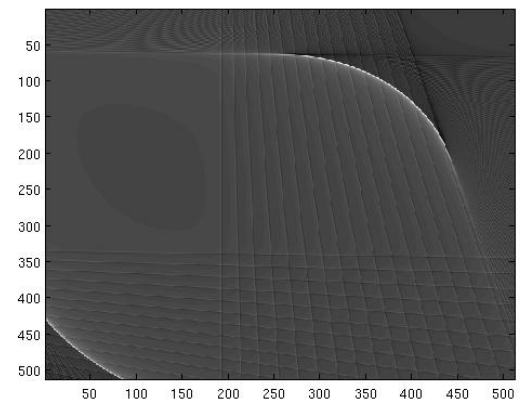
Figure 3.37: Limited angle reconstruction performed from $0° \rightarrow 90°$.
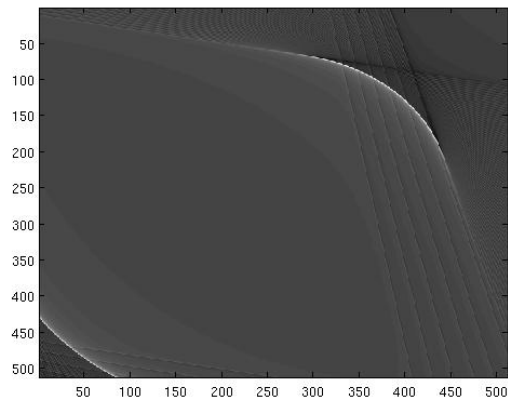
Figure 3.38: Limited angle reconstruction performed from $10° \rightarrow 80°$.
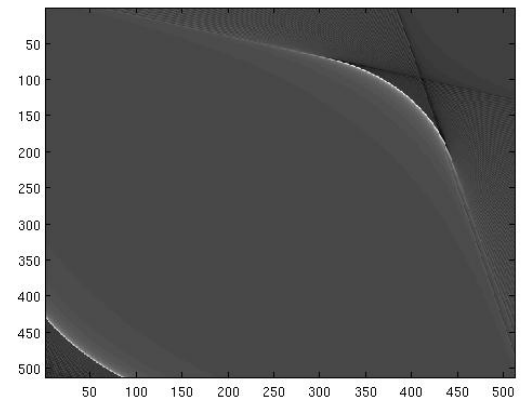
Figure 3.39: Limited angle reconstruction performed from $15° \rightarrow 75°$.

Figure 3.40: Photograph of the Rando head, with reconstruction region identified.
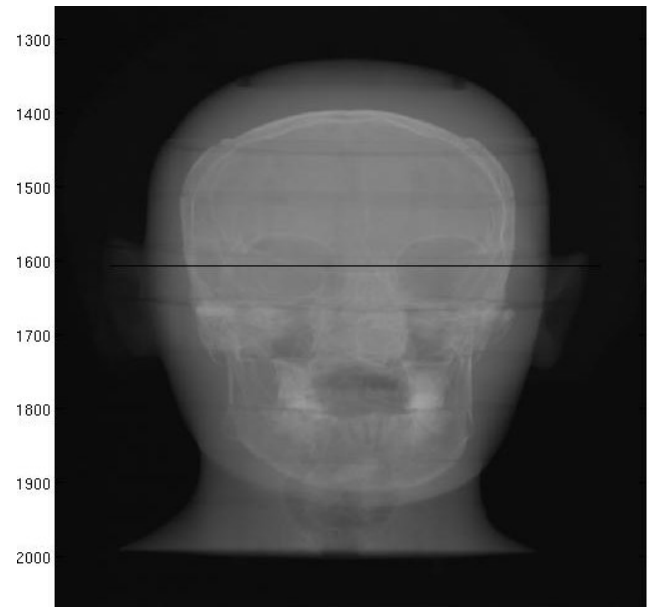
Figure 3.41: Anteroposterior X-ray image of the Rando head, with reconstruction row identified.
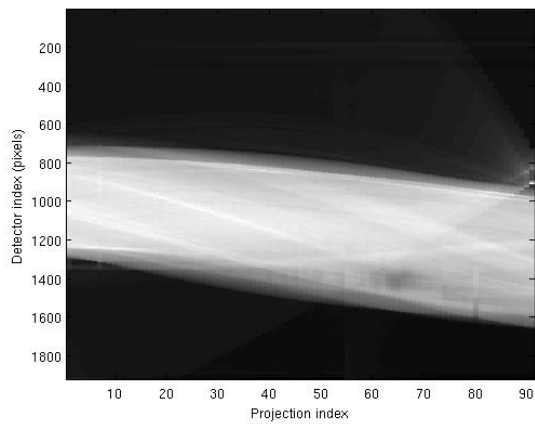
Figure 3.42: Lodox sinogram, first scan set.
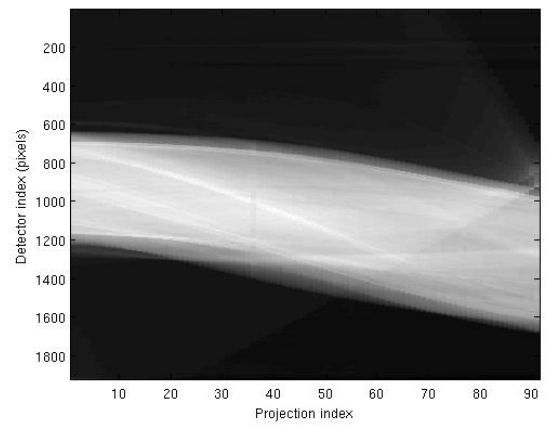
Figure 3.43: Lodox sinogram, second scan set.
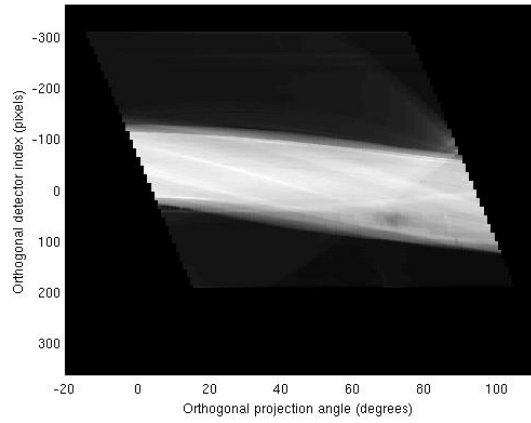
Figure 3.44: Sinogram, first scan set. $\theta = (-20°; 120°)$.
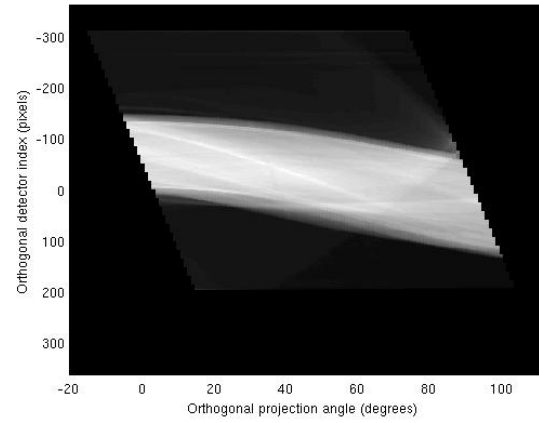
Figure 3.45: Sinogram, second scan set. $\theta = (-20°; 120°)$.
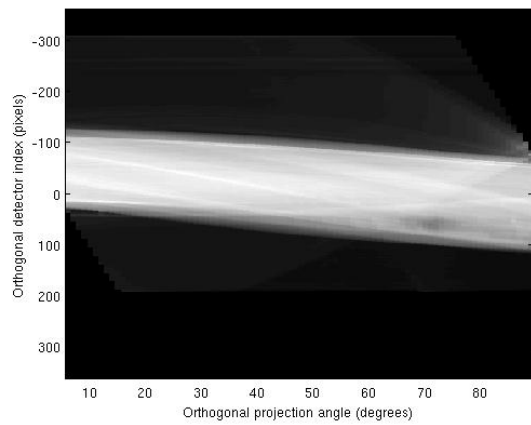
Figure 3.46: Sinogram, first scan set. $\theta = (6°; 89°)$.
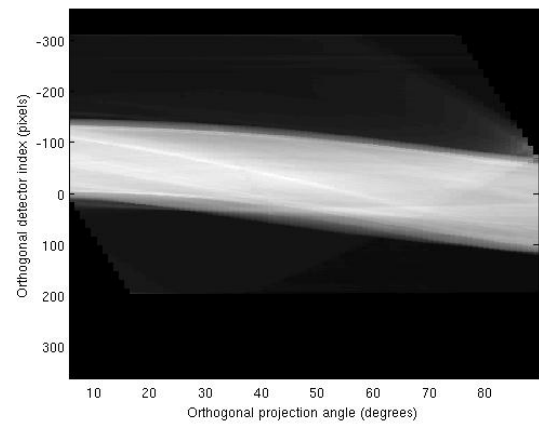
Figure 3.47: Sinogram, second scan set. $\theta = (4°; 88°)$.
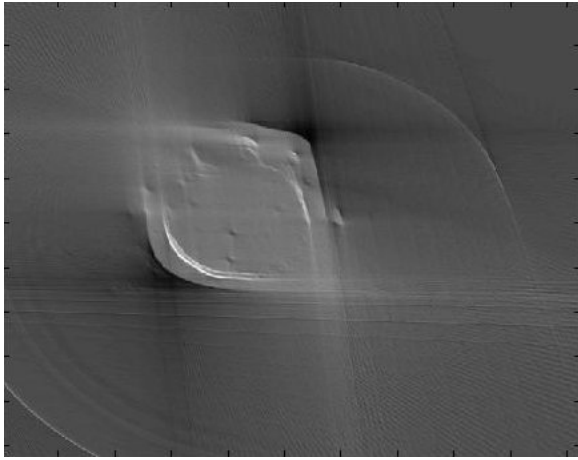
Figure 3.48: Filtered back projection, first scan set.
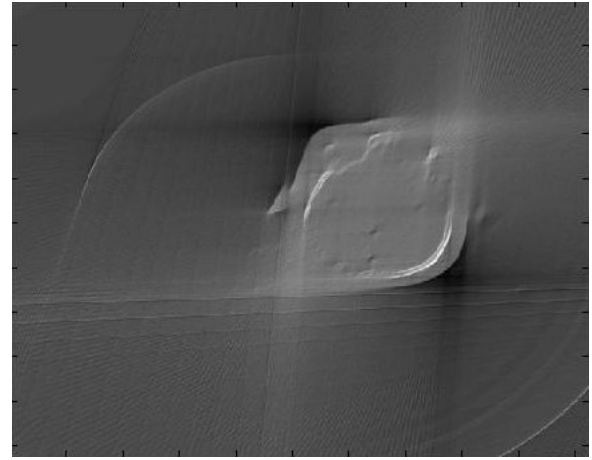
Figure 3.49: Filtered back projection, second scan set.
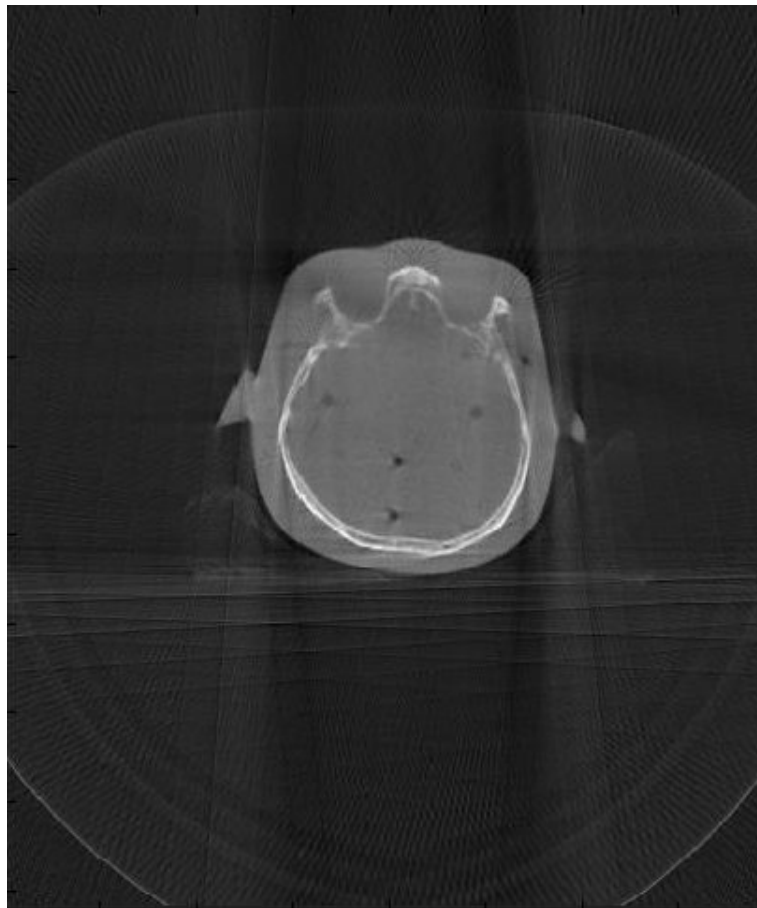
Figure 3.50: Filtered back projection, half reconstructions correlated and summed.

Chapter 4

Subsystem and system level experiments

This chapter contains different types of tests which span both subsystem and system level testing. The subsystem level testing done is to verify that the automated image processing methods are effective at detecting the markers and can estimate the marker positions accurately (Sections 4.1–4.4). The system level testing is done in three separate ways; firstly, reprojections are made of the reconstruction and the two projections are compared in terms of a reprojection error using points, normalised cross correlation and the comparison of sinogram intensities (Sections 4.6–4.8). The second set of system level testing is performed on the actual reconstruction images by comparing information extracted from the reconstruction image to measurements known a-priori, such as the 3D reconstruction accuracy, the uniformity of the CT number when scanning homogeneous material and the high contrast resolution of the reconstruction (Sections 4.9–4.11). The last section is a report of the computing time taken to generate a reconstruction set from the projection data (Section 4.12).

The performance of the top-of-image alignment procedure is established using two tests: the top-of-image marker detection which is a hit-or-miss metric of the number of markers that are correctly identified (Section 4.1) and the top-of-image alignment accuracy which is an error metric comparing the approximated marker positions to a ground-truth manually annotated set of marker positions (Section 4.2). All of the markers were correctly detected with a high accuracy, having an RMS error of 1 pixel.

The performance of the automatic procedure for finding the positions of the calibration markers is also established with two similar tests, a hit-or miss calibration marker detection test (Section 4.3) and the calibration marker identification accuracy test (Section 4.4). A detection rate of 96% of the calibration markers was achieved with the automatic method, with the causes of the failure cases explained. The position of correctly detected calibration markers is accurately detected by the automated method, with 96% of the calibration marker positions being estimated to withing $\epsilon < 1.0$ and 99% to within $\epsilon < 1.5$.

The c-arm angles that are manually read from the Lodox control computer are compared the the C-arm angles produced by the calibration is a measure of how well the calibration optimization was performed. As the manually read angle has a resolution of 1° and the optimization is more precise, an error of less than 0.5° is not significant and as the average RMS error is 0.2° and the maximum error is 0.51°, the angles are regarded as being correctly approximated.

The reprojection error experiment (Section 4.6) is a test of how well the reconstruction represents the subject, performed by projecting discrete points from a reconstruction onto a detector line and comparing the software projected positions to the positions of the same features on the original projections, producing values that appear large ($\epsilon_{max} \approx 20$ pixels), but which are exaggerated by the relative resolution of the detector to the reconstruction as well as the projective nature of the system.

A normalised cross correlation of the original Lodox sinogram with the reprojection of a Lodox sinogram gives another reprojection based measure of how well the reconstruction represents the subject based on the overall image intensity. The normalised cross correlation produced a very high result of 0.988. The last metric used to compare the original projection to the reprojection of the reconstruction is comparing the histograms of the Lodox sinogram and the reprojected sinogram (Section 4.8). This is a subjective comparison and the two histograms have a very similar appearance one a $2\times$ scaling of pixel intensities is accounted for.

Verifying the spatial accuracy of the tomographic reconstruction reconstruction is done by comparing distance measurements made on a physical device to corresponding measurements made from tomographic reconstruction images (Section 4.9). The mean error encountered is *1.1 pixels* with standard deviation $\sigma = 0.88$.

The consistency of a reconstruction of uniform materials (both air and water) gives an indication of the error that can be expected in the intensity values of a reconstruction (Section 4.10). The Lodox tomographic reconstructions are inferior to commercial CT scanner values, having approximately $10\times$ the maximum allowable variation in the intensity of a reconstruction of a homogeneous material.

A high-contrast phantom with regions of different spatial resolution was included in the scan data, where the finest set of markers that can be identified indicates the spatial resolution of the reconstruction (Section 4.11). This test failed as the resolution of the reconstructions generated was lower than the most coarse markers in the phantom.

The computation time to produce a reconstruction set of 1000 slices on two different hardware platforms is tested (Section 4.12) and 1000 slices can be reconstructed on a high-end desktop computer in a little over 1 hour.
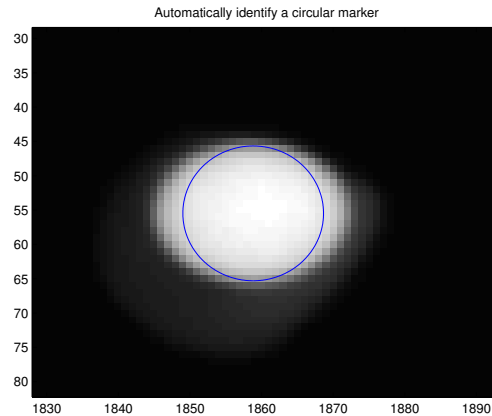
Figure 4.1: Successful automatic top of image marker identification.

4.1 Top-of-image marker detection

The automatic algorithm for identifying the top-of-image markers (in Section 3.3) produces a row index for each of the images in a projection set. The effectiveness of this automated method at correctly detecting the top-of-image markers needs to be established.

4.1.1 Procedure

The automatic function for finding the centre of a top-of-image marker (Section 3.3.3) has a built-in test feature where a circle is drawn on top of the identified marker which is performed on each of the 182 images used in this study (2 sets of 91 images), an example of which is shown in Figure 4.1. Successful identification is verified by eye using the marker image and an overlaid circle centred at the result of the automatic procedure.

4.1.2 Results

For the angular range $0° \rightarrow 90°$ (the first scan set) and for the angular range $0° \rightarrow -90°$ (the second scan set), all of the top-of-image markers were identified correctly. No failure modes were encountered and the detection capability of the automated method is robust for implementation.

4.2 Top-of-image accuracy

The automatic algorithm for identifying the top-of-image markers (in Section 3.3) produces a set of row indices for each projection set. The accuracy of this process in estimating the centre of the each top-

	Scan set 1	Scan set 2	combined
Maximum absolute error, $max\lvert\epsilon_i\rvert$	1.96	1.88	1.96
RMS error, $\frac{1}{N}\sum_i^N \lvert\epsilon_{top\text{-}of\text{-}image,\ i}\rvert$	1.14	0.88	1
σ_{error}	0.4	0.4	0.4

Table 4.1: Top of image alignment error measures.

of-image marker needs to be established. The experiment performed here is a position accuracy test, where the centre points of the markers that are identified by the automatic algorithm are compared to the centres of a manually-annotated reference set.

4.2.1 Procedure

A manually-annotated control set is required, this is generated by manually identifying the centre of the top-of-image markers on each image. The manual-annotation procedure is performed as follows:

- for each image the MATLAB function *dicomread* is used to read the files into memory,

- the *imagesc* function is used to display the images, and the region containing the top-of-image marker is expanded using the zoom function,

- the centre of the marker on each X-ray projection image is identified by eye and the mouse cursor is placed at this point,

- the image viewer displays the pixel location, and

- this pixel location is manually recorded into a spreadsheet.

The difference between the row values of the manually identified marker centres and the row values returned from the automatic top-of-image marker identification procedure indicates how well the automated function is operating.

4.2.2 Results

The error metric, $\epsilon_{(top\text{-}of\text{-}image,\ i)} = row_{(manual,\ i)} - row_{(automatic,\ i)}$, produces a marker row identification error value for each projection image. Scatter plots of these error points are shown in Figure 4.2 for scan set 1 and in Figure 4.3 for scan set 2.

These errors can also be represented as the statistical measures in Table 4.1.

The top-of-image errors present should not jeopardise the image reconstruction, as the maximum error encountered ($705\mu m$=1.96 pixels $\times\, 360\mu m$) is small relative to the reconstruction pixel size ($1mm$). That all of the errors are positive could indicate a systematic bias in the manual reading technique.
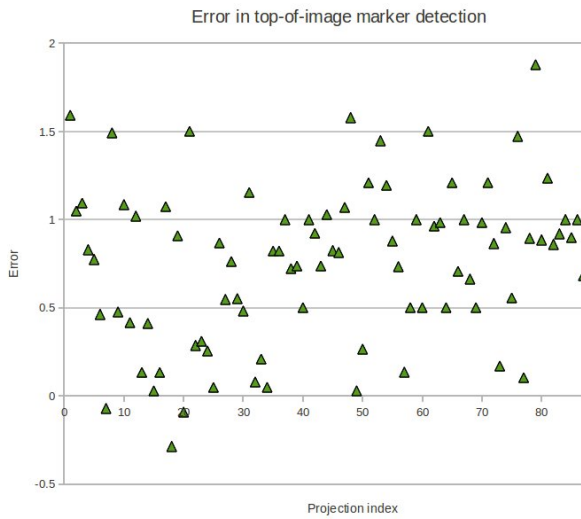
Figure 4.2: Top-of-image errors–first scan set.   Figure 4.3: Top-of-image errors–second scan set.
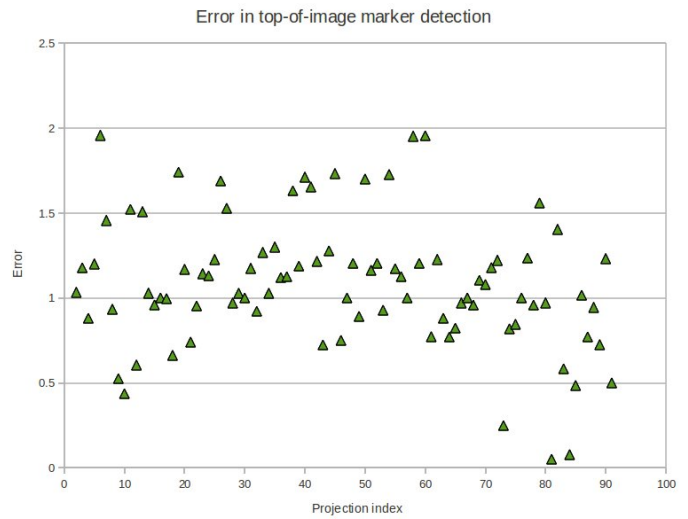
4.3   Calibration marker detection

The automatic procedure for identifying each of the calibration marker pins (described in Section 3.4.4) produces three column indices per projection image, one for each of the three calibration markers. The performance of this procedure needs to be established. The experiment performed here aims to test the sensitivity of calibration marker identification.

4.3.1   Procedure

A graphical output mode has been built into the automatic function that identifies the calibration markers in an image. It produces an intensity plot of the row in which the calibration markers are identified, as well as markers in columns that are identified as being at the middle of a calibration marker by the algorithm. Successful identification is verified by eye by checking that the cross marking the middle of a marker coincides with an intensity peak (Figure 4.4).

4.3.2   Results

For the both the angular ranges $0° \rightarrow 90°$ and $0° \rightarrow -90°$, $\left(\frac{87}{91}\right)$ images had all three markers correctly identified, corresponding to a sensitivity of 96%.

For both scan sets, the failure cases all occurred for projections at and nearest to the lateral projection (from the 88th projection to the 91st projection). Comparing the 87th and the 88th image of the first scan set indicates causes of failure (Figures 4.4 and 4.5); in the 88th image the intensity of the table projection has a maximum value of 3265 which is higher than the threshold intensity (3000), a second
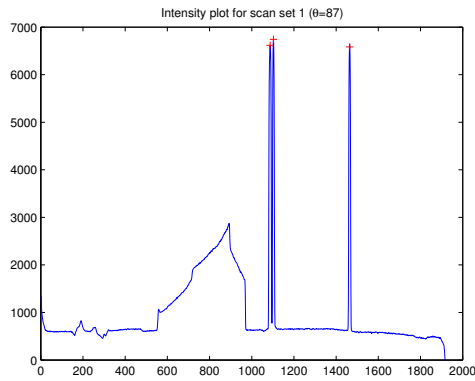
Figure 4.4: Intensity plot for scan set 1 projection 87.
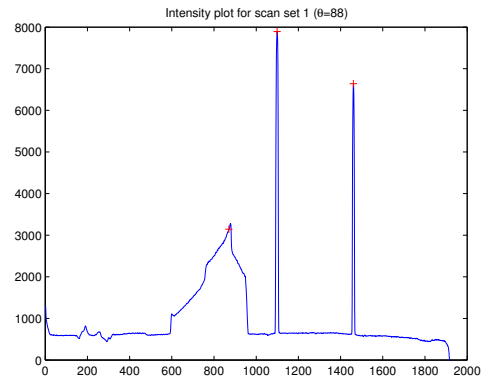
Figure 4.5: Intensity plot for scan set 1 projection 88.
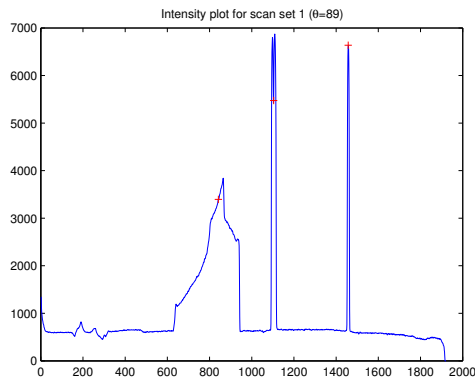
Figure 4.6: Intensity plot for scan set 1 projection 89.
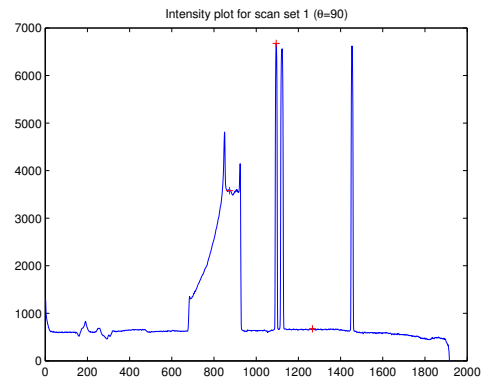
Figure 4.7: Intensity plot for scan set 1 projection 90.

reason why this image would cause the method to fail is that the two calibration markers on the left-hand side occlude one another.

The 89th and 90th projections of the first scan set also fail due to the intensity of the table being greater than the threshold used (Figures 4.6 and 4.7). The intensity of the table projection increases as the c-arm angle approaches 90°, reducing the contrast between the projected calibration marker and the background. In both of these projections, three projected pins are clearly visible. The 91st projection, generated at a c-arm angle of $\theta_{\text{c-arm}} = 90°$, also fails due to the projection of the table having a higher intensity than the threshold value. In this case the projected intensity of the table is larger then the projected intensity of the calibration marker (Figure 4.8).

The projections the two calibration markers at approximately column 1100 are swapped between the 87th image and the 91st image of the first data set (Figures 4.4 and 4.8), this would also cause the current automated marker identification procedure to fail even of the threshold been selected at a higher value. This projected position swap also occurs in the second data set.
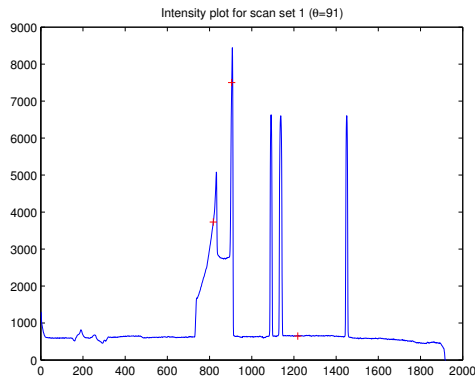
Figure 4.8: Intensity plot for scan set 1 projection 91 ($\theta_{\text{c-arm}} = 90°$).

Projection	Peak table intensity	Average peak marker intensity	Markers occlude or swap position
set 1, 88	3264	7477	occlude
set 1, 89	3832	6753	swap
set 1, 90	4700	6584	swap
set 1, 91	8444	6608	swap
set 2, 88	2880	6756	occlude
set 2, 89	3343	7652	occlude
set 2, 90	4047	6772	swap
set 2, 91	4887	6676	swap

Table 4.2: Calibration marker failure modes.

A summary of the failure modes for the first and second scan sets is included in Table 4.2.

Adjusting the threshold to a higher value, possibly a dynamic threshold based on image intensity, would allow for more robust marker identification. The cases where markers occlude one another or swap position requires a more intelligent calibration marker identification procedure or more precise placement of the calibration markers such that markers cannot occlude one another.

4.4   Calibration marker identification accuracy

The automatic calibration marker identification function in Section 3.4.4 produces 3 column indices per projection image, one for each of the three calibration markers. The accuracy of this automatic procedure in estimating the position of each of the calibration markers needs to be established. This is done by comparing centre column of the each marker in each image as identified by the automated method to the centre of each marker in a manually-annotated reference set. As the accuracy measurement is only relevant in cases where the detection has been successful, the cases where marker identification failed are omitted.

ϵ	Number in $0° \to 90°$	Number in $0° \to -90°$	Number in $-90° \to 90°$	Cumulative percentage
$0 \leq \epsilon < 0.5$	115	140	255	49%
$0.5 \leq \epsilon < 1$	133	114	237	96%
$1 \leq \epsilon < 1.5$	10	7	17	99%
$1.5 \leq \epsilon < 2$	3	0	3	100%
$2 \leq \epsilon$	0	0	0	100%

Table 4.3: Error frequency table.

4.4.1 Procedure

A manually-annotated control set is required. The same image row was used to generate this ground-truth as was used by the automatic calibration marker identification procedure. For each of the images in the dataset, the intensity of a row containing the calibration markers is plotted using MATLAB's *plot* function. On this image, the mouse cursor is moved to the rising edge and falling edge of each major spike in the intensity plot. The values are manually read off and the mean pixel between the rising and falling edges is regarded as the manually annotated calibration marker projection midpoint.

The automatic calibration marker procedure described in Section 3.4.1 produces three column indices per projection image. These are compared to manually annotated marker midpoints to generate an error metric

$$\epsilon_{\theta_i} = [x_{(man,1)} - x_{(auto,1)}, x_{(man,2)} - x_{(auto,2)}, x_{(manual,3)} - x_{(auto,3)}]. \tag{4.1}$$

Both the first and second scan sets will each have a metric that consists of a total count of 87 projections and 261 calibration markers.

4.4.2 Results

The frequency of occurrence of ranges of pixel errors is presented in Table 4.3, and shows that 96% of the markers are found with less than 1 pixel error. All of the non-zero error values had a positive magnitude, more likely indicative of a measurement biasing in the annotation of the ground-truth values rather than of a characteristic of the automatic method.

4.5 C-arm angle approximation

A measure of how well the optimization is being performed can be generated by comparing the C-arm angles as produced by the optimisation process with the c-arm angles as produced by a control set of C-arm angle values manually recorded from the Lodox control computer during the scan procedure.

4.5.1 Procedure

For both the scan sets $0° \rightarrow 90°$ and $0° \rightarrow -90°$ the C-arm angle was manually set in 1°increments, the control set of C-arm angles is 0°,1°,2°,...,89°, 90° and $0°, -1°, -2°,..., -89°, -90°$. These manually read control angles have 1°resolution. The optimisation process produces a C-arm angle for each of the projections, these angles are produced with a floating point precision, these are rounded to the nearest integer to give the same resolution as the control set.

4.5.2 Results

For the $0° \rightarrow 90°$ scan set, $\frac{90}{91}$ of the C-arm angles were approximated having a negligible angle ($\epsilon < 0.5$ when $\theta_{auto} \subset \mathbb{R}$ and $\epsilon = 0$ when $\theta_{auto} \subset \mathbb{Z}$).

The one non-negligible error was $\epsilon_{\theta=10°} = 0.512$ with $\theta_{auto} \subset \mathbb{R}$.

4.6 Reprojection error using points

A numerical approximation of how well a tomographic reconstruction represents the subject can be made by generating a reprojection error, this is where reprojections of the reconstruction are performed and compared to the original projection data. In this case solid markers are used and are considered as points in both the reconstruction (at the centre of reconstructed calibration marker pin) and in the original projection data (middle pixel of the projected calibration marker pin).

4.6.1 Procedure

To generate three projected marker indices for the real image data, a row with non–overlapping markers has a threshold function applied and a centre value is found for each of the regions with pixel intensity exceeding the threshold value. Producing the three reprojected marker indices for the same projection angle is performed using a software forward–projection of the reconstruction, with the model's c-arm angle set to the estimated c-arm angle produced by the optimisation of the cost function (Section 3.4.5).

The distance between the median of a true projected marker and the simulated projection of the reconstruction is the error for that particular marker.

4.6.2 Results

Slice 100 is selected as it has three high contrast markers in the image. For 10 projections spaced at approximately every 10° the mean value of a pin projection on the real data is compared to the mean

Lodox sinogram row	ϵ_{pin1}(pixels)	ϵ_{pin2}(pixels)	ϵ_{pin3}(pixels)	$RMSE(\epsilon, \theta)$
scan set 1, $\theta = 1°$	2.5	1.5	3.5	1.9
scan set 1, $\theta = 11°$	1	4.5	5.25	3.2
scan set 1, $\theta = 21°$	4.5	5	7.5	5.0
scan set 1, $\theta = 31°$	8	12	9.75	9.4
scan set 1, $\theta = 41°$	10	13.925	12.25	11.5
scan set 1, $\theta = 51°$	11	11.5	13.75	11.3
scan set 1, $\theta = 61°$	14	13	15	13.5
scan set 1, $\theta = 71°$	14.5	14	17.25	14.5
scan set 1, $\theta = 81°$	15.5	14	21.5	15.7
scan set 1, $\theta = 91°$	18	15.5	24	18.5

Table 4.4: Slice 100, scan set 1, reprojection errors for markers.

Lodox sinogram row	ϵ_{pin1}(pixels)	ϵ_{pin2}(pixels)	ϵ_{pin3}(pixels)	$RMSE(\epsilon, \theta)$
scan set 2, $\theta = 1°$	-3	-1.5	5	3.5
scan set 2, $\theta = 11°$	0	-1.5	5.5	3.3
scan set 2, $\theta = 21°$	0.5	-1.5	4	2.5
scan set 2, $\theta = 31°$	4	-2.5	3	3.2
scan set 2, $\theta = 41°$	6.5	-3	1.5	4.2
scan set 2, $\theta = 51°$	11.5	-2.5	1	6.8
scan set 2, $\theta = 61°$	12	-3	-0.5	7.1
scan set 2, $\theta = 71°$	16	-3.5	-2.5	9.6
scan set 2, $\theta = 81°$	18.5	-4	-5	11.3
scan set 2, $\theta = 91°$	2	12	-5	7.6

Table 4.5: Slice 100, scan set 2, reprojection errors for markers.

value of a reprojection of the tomographic reconstruction, and an error measure is calculated to represent the difference (Table 4.4 and Table 4.5).

The overall error measures for scan set 1 and scan set 2 are:

$$RMSE_{scanset1} = 10.3 \, \text{pixels}$$

$$RMSE_{scanset2} = 4.7 \, \text{pixels}$$

The *RMSE* per angle is lower for the images closer to AP and increases as the lateral view ($\theta = 91°$) is approached.

The reprojection errors are large values, this is because they are magnified by the projective nature of the X-ray imaging platform and the relative resolution of the physical detector to that of the reconstruction.

A 1-pixel perturbation at the centre-of-rotation leads to a change in the projection of

$$\frac{d}{d_r} \times \frac{a_{reconstruction}}{a_{detector}} = \frac{1253mm}{995mm} \times \frac{1mm/pixel_{reconstruction}}{0.36mm/pixel_{projection}} = 3.5 \, pixel_{projection}/pixel_{reconstruction},$$
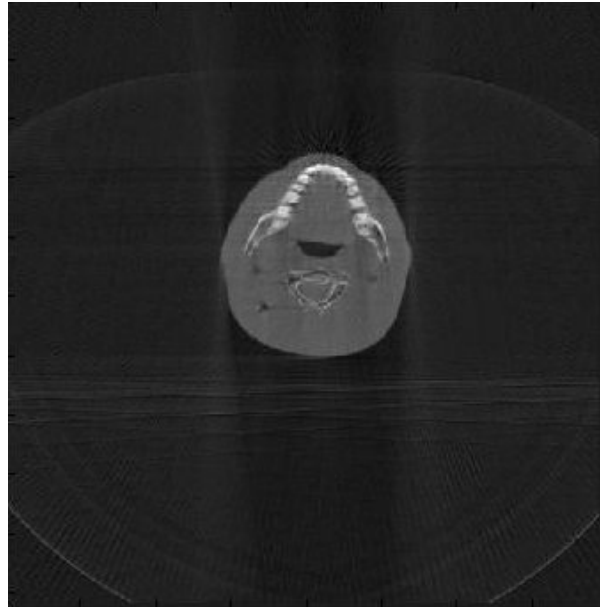
Figure 4.9: Reconstruction of Rando phantom, row 1825.

which means that for every 3.5 pixels of error in the reconstruction, approximately 1 pixel error is present in a direction perpendicular to the X-ray projection.

4.7 Normalised cross correlation

Anatomical image reconstruction contains more than just the location of discrete points. Comparing an original projection to the reprojection of the slice reconstruction can be used as a metric to test the reconstruction accuracy.

The cross correlation of the original Lodox sinogram with a reprojected reconstruction Lodox sinogram is the method used to compare the reconstruction accuracy for a single slice over an entire projection set.

4.7.1 Procedure

The region reprojected is the maxilla region of the Rando imaging phantom (Figure 4.9), the original Lodox sinogram has a very similar appearance to the reprojected Lodox sinogram (Figures 4.10 and 4.11).

The maximum value of a two-dimensional normalised cross correlation of a Lodox projection image with the reprojected reconstruction will give a measure of the similarity of the two. The closer the normalised cross correlation (ρ) is to 1, the more similar the two images are to one another.
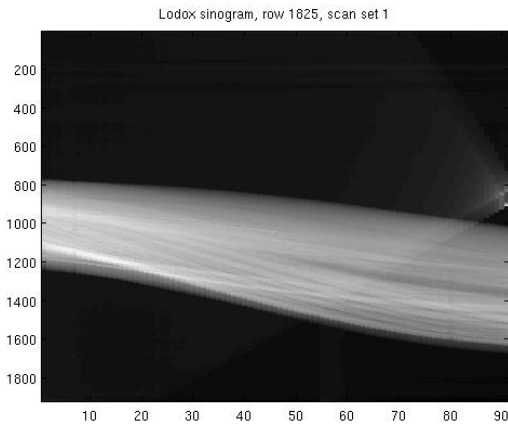
Figure 4.10: Lodox sinogram of the Rando phantom, scan set 1, row 1825.
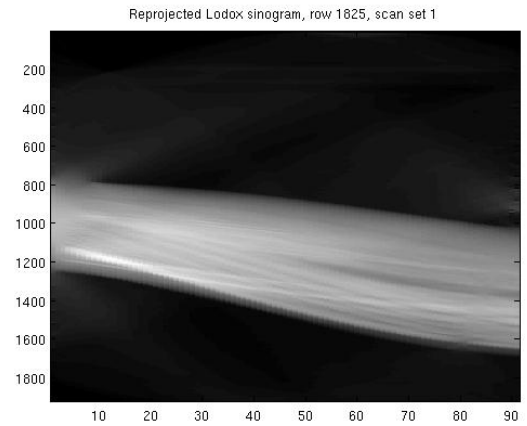
Figure 4.11: Reprojected reconstruction of the Lodox sinogram of the Rando phantom, scan set 1, row 1825.

4.7.2 Normalised cross correlation–Results

A visual check of the Rando sinograms (Figure 4.10) and the reprojection of its reconstruction (Figure 4.11) shows that they are very similar. The normalised cross correlation produced a maximum value of 0.9883.

4.8 Comparison of sinogram intensities

In addition to the normalised cross correlation (Section 4.7), it is useful to compare the actual Lodox Sinogram intensities to the sinograms intensity of a reprojected reconstruction. This should show whether significant intensity scaling or nonlinear distortion has occurred.

4.8.1 Procedure

The intensity range of the Lodox sinogram and the reprojection of its reconstruction are compared visually and comments are made regarding the range and distribution of the intensity levels. This is performed using histograms of the pixel intensity values.
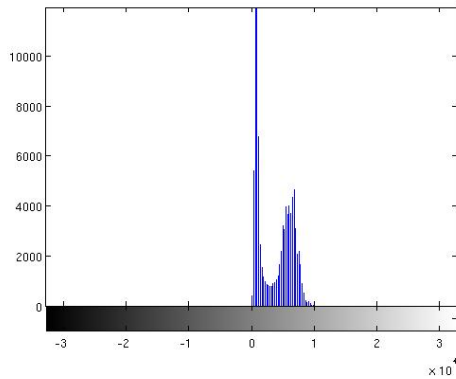
Figure 4.12: Histogram of the Lodox sinogram in Figure 4.10.
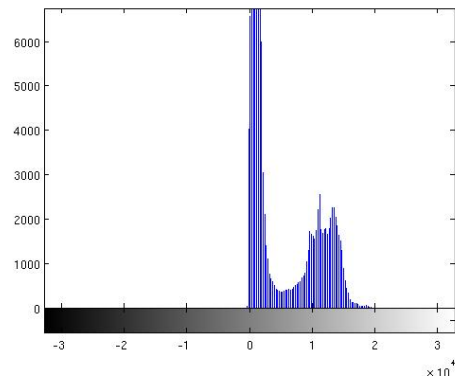
Figure 4.13: Histogram of the reprojected reconstruction Lodox sinogram in Figure 4.11

4.8.2 Results

A histogram of the Lodox sinogram (Figure 4.10) is shown in Figure 4.12, and the histogram of the reprojected reconstruction of the Lodox sinogram (Figure 4.11) is presented in Figure 4.13. The intensity values of the reprojected reconstruction sinogram span an intensity range approximately twice as wide as that spanned by the original sinogram, and the number of elements is also reduced by about half.

A fairly linear scaling (effectively a doubling of each intensity value) of the intensities has occurred. This is due to the summation of the $0° \rightarrow 90°$ half-reconstruction with the $0° \rightarrow -90°$ half-reconstruction, which is different to averaging behaviour of a filtered back-projection algorithm.

4.9 3D reconstruction accuracy

A useful feature in tomographic reconstruction is that the reconstruction image provides a geometrically accurate representation of the subject that is being imaged. To test the geometric accuracy of the Lodox tomographic reconstructions, a phantom with small radio-opaque markers is included in the scan set. The marker coordinates are known for the phantom and are measured from the reconstruction data.

The Euclidean distances from each marker to every other marker are calculated for both ground truth and image acquired measurement sets. The difference between each of these two sets of distance measurements is calculated and metrics are produced to assess the reconstruction accuracy.

4.9.1 Procedure

A rigid 3D phantom is included in the scan set (Figures 3.5 and 3.6). The ground-truth 3D location of small metal balls in this device are known reliably, measured to 1μm precision using a stereo-tactic microscope. The positions of the balls are manually identified in the reconstructed images in terms of coordinates in the slice and the slice index, which are transformed into 3D coordinates to produce the tomographic reconstruction position measurements. Since an arbitrary rotation and translation is present between the ground-truth measurements and the measurements taken from the reconstructions (due to two different and uncalibrated coordinate frames being used), Euclidean distances between points are used to compare the similarity of the two 3D coordinate sets.

Specifically, there are 15 balls labelled 1,2,..,15. Distance measurements from each ball to every other ball will quantify the accuracy of reconstruction in 3D (i.e ball 1 to balls 2,3,...,15, ball 2 to balls 3,4,...,15 and ball 3 to balls 4,5,...,15 and so on). If (x_i, y_i, z_i) are the ground-truth coordinates of the ith metal ball as measured with the microscope and (p_i, q_i, r_i) are the coordinates of the same ball measured from the tomographic reconstruction. The error in the distance from the i_{th} ball to the j_{th} ball is

$$\epsilon_{(i,j)} = \left(\sqrt{(x_i - x_j)^2 + (y_i - y_j)^2 + (z_i - z_j)^2} - \sqrt{(p_i - p_j)^2 + (q_i - q_j)^2 + (r_i - r_j)^2} \right).$$

As the 512 pixel reconstruction will have a spatial resolution of $1mm/$pixel and the slices are $0.36mm$ apart, the maximum expected precision is

$$\varepsilon_{min} = \sqrt{\left(\frac{1}{2}\right)^2 + \left(\frac{1}{2}\right)^2 + \left(\frac{0.36}{2}\right)^2} = 0.73mm.$$

4.9.2 Results

A total of 105 distance measures are calculated (between each ball and every other ball) using both sets of data and the *root mean square error* is $1.11mm$ with a standard deviation of 0.88. Individual errors measured are presented graphically in Figure 4.14.

Tomographic reconstruction performed with a Lodox Statscan produces a fairly good representation of the subject being scanned, but with a maximum error encountered of $3.18mm$ measurements made can only be trusted to be accurate to the nearest $3mm$.

4.10 Measuring the uniformity of CT numbers

The tomographic reconstruction of a homogeneous medium should be an image region with uniform intensity. In a CT scanner the average intensity of air and water is used to calibrate the CT number
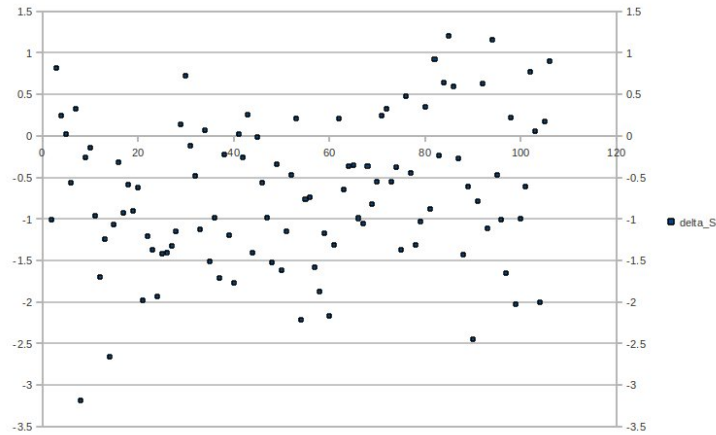
Figure 4.14: Error in measuring lengths on the 3D phantom.

to Hounsfield units. The uniformity of the reconstruction is a quality assurance metric for tomographic reconstruction.

A Catphan® commercial quality assurance CT phantom with solid cast uniformity module, a region of plastic that is made to have a uniform CT number to within 2% of water is included in the reconstruction sets as the water phantom region. Slices with no objects to reconstruct are used as air phantom region. The mean and standard deviation of water and air in different slices indicates the consistency of the reconstruction.

The intensities used for these measurements are the pixel intensities as returned by the filtered back projection algorithm. No intensity calibration has been performed and the values are considered to be of an arbitrary intensity units.

4.10.1   Procedure

Three slices containing the Catphan CT uniformity module (water phantom) are selected, 20 pixels apart, and on each of these 5 regions of 100 pixels (10 × 10) are selected. The mean and standard deviation of these pixels are calculated (Figure 4.15).

To generate an equivalent set of measurements for air, the same method of selecting three slices is performed. To sample air, the slices are selected in a scan region where there are no features scanned other than the scan table.

The mean and standard deviation are calculated both within each 100 pixel block as well as between the blocks.

	Slice index	mean (water)	standard deviation (water)	Slice index	mean (air)	standard deviation(air)
Slice A, Block 1	2380	78.4	2.1	2030	2.1	0.7
Slice A, Block 2	2380	79.4	1.7	2030	2.1	0.5
Slice A, Block 3	2380	79.9	2.2	2030	2.0	0.8
Slice A, Block 4	2380	80.2	2.4	2030	2.1	0.7
Slice A, Block 5	2380	80.3	2.2	2030	2.1	0.7
Slice B, Block 1	2400	78.3	2.1	2050	2.1	0.8
Slice B, Block 2	2400	79.4	2.0	2050	2.2	0.7
Slice B, Block 3	2400	79.9	2.2	2050	2.0	0.7
Slice B, Block 4	2400	79.8	2.2	2050	2.1	0.7
Slice B, Block 5	2400	80.5	2.0	2050	2.0	0.8
Slice C, Block 1	2420	78.7	2.1	2070	2.1	0.7
Slice C, Block 2	2420	79.3	2.0	2070	2.2	0.7
Slice C, Block 3	2420	79.7	2.2	2070	2.0	0.8
Slice C, Block 4	2420	80.0	2.2	2070	2.1	0.7
Slice C, Block 5	2420	80.3	2.1	2070	2.1	0.8
overall	n/a	79.6	0.69 (of the means)	n/a	2.14	0.42 (of the means)

Table 4.6: Mean intensity and standard deviation for air and water regions.
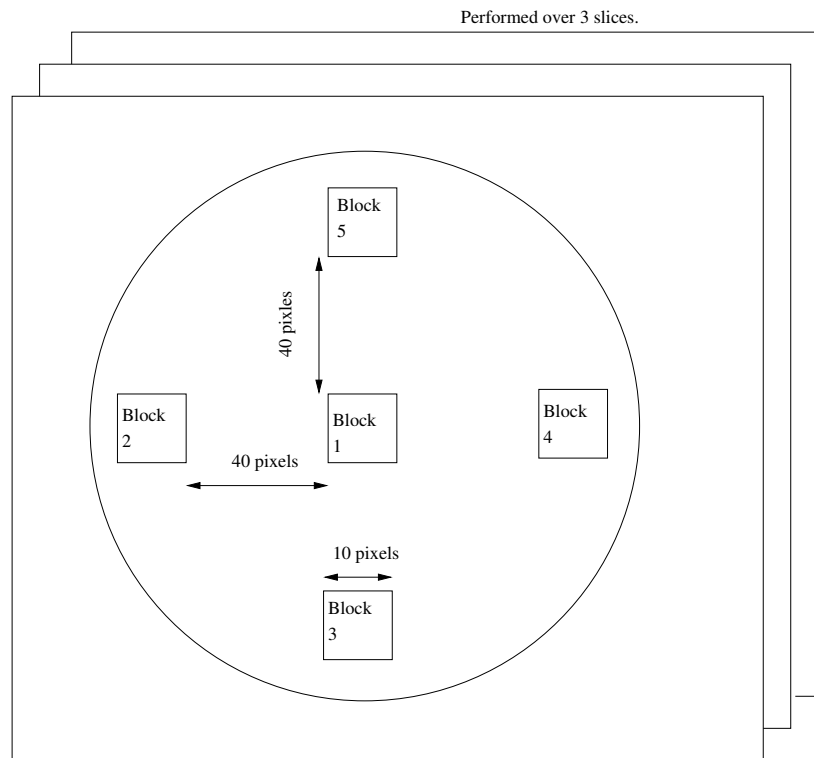
Figure 4.15: Water and air phantom regions for CT number consistency measurement.

4.10.2 Results

The intensity is initially appears quite consistent between regions on the same slice as well as across different slices but a quantitative measure is required. In order to compare the consistency of reconstructions performed on Lodox Statscan images to the that expected for a commercial CT scanner, the Lodox reconstructions will to checked against quality CT scanner assurance standards.

For a commercial CT scanner, CT number for water should be 0 ± 3 and it should have a standard deviation of no more than 10. The CT number for air should be -1000 ± 5 (Bushong, 2000). Scaling these Hounsfield unit based bounds to the uncalibrated range produced using the Lodox Statscan produces transformed bounds (i.e. from water at 0 and air at -1000 to water at 79.6 and air at 2.14), pixels of the water phantom should be in the range 79.6 ± 0.23 and air should be in the range 2.14 ± 0.39. The standard deviation of water should be less than $\sigma = 0.775$.

The consistency of the Lodox tomographic reconstructions are inferior to commercial CT scanner quality standards, errors and standard deviation are too high by one order of magnitude.
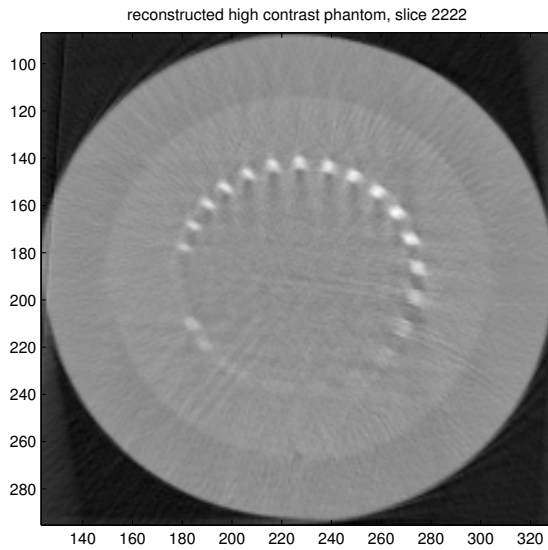
Figure 4.16: Reconstructed of the high contrast resolution phantom.
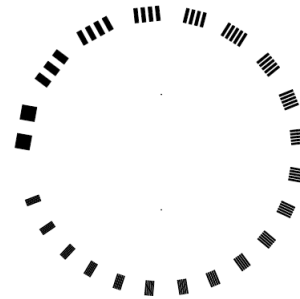
Figure 4.17: Diagram of the high contrast resolution phantom.

4.11 High contrast resolution

The maximum resolution of high contrast markers that can be reconstructed by a tomographic reconstruction procedure is a value representative of the finest anatomical detail identifiable in a reconstruction image.

4.11.1 Procedure

By examining reconstructions of a high contrast resolution phantom and identifying the smallest feature present in the image, a measure of the highest spatial resolution that can be reconstructed can be found.

4.11.2 Results

Performing a filtered back-projection of a projected slice containing the high contrast resolution phantom produces an image where the high contrast markers are visible (Figure 4.16). Determining the minimum contrast for successful reconstruction was not possible as correspondence between the reconstruction of the phantom (Figure 4.17) could not be established. The progression from lower resolution markers to higher resolution markers occurs in a counter-clockwise rotation from the 9 O'clock position, opposite to the diagram (Figure 4.17). More detail can be seen in the higher resolution markers than in the lower resolution markers, most likely due to the projection data being limited to 180°.

Platform	Laptop computer	Desktop PC
CPU	Intel core 2 duo (dual core 2.4GHz)	Intel i7 920 (quad core 2.6GHz)
RAM	4GB	6GB
Operating system	Ubuntu Linux 10.04 x64	Ubuntu Linux 10.04 x64
Matlab version	R2009b	R2009b

Table 4.8: Computer specifications.

Platform	Laptop computer	Desktop PC
Loading images	90s	39s
Finding System parameters	41s	24s
Reconstruction (per slice)	8.33s	3.81s
Total time for 1000 slices	*2.3 hours*	*1.1 hours*

Table 4.9: Computation time.

4.12 Computation time

The time it takes for a computer to produce a set of tomographic reconstructions from projection data is an important metric. Reasonable reconstruction times are required if Lodox tomography is to be feasible in a forensics setting or as a tool to be used for research. Time take to perform the marker identification, system model optimisation, reprojection and reconstruction was recorded for both a high-end desktop computer workstation as well as for a medium range laptop computer. Both platforms were adequate platforms for performing individual slice reconstruction, but a large volume reconstruction (hundreds of slices) would best be done on the high-end desktop workstation.

4.12.1 Procedure

The time taken to perform the different stages of the reconstruction process is recorded, as is the total time taken to generate a reconstruction. Tests were performed on two separate hardware platforms, a high-end desktop computer and a medium range laptop computer (Table 4.8).

4.12.2 Results

Results are presented in Table 4.9. Reconstruction of selected slices can be performed on either hardware platform. The time taken to produce a 1000-slice reconstruction set (1000 slices at 1mm apart) would take just over an hour on a single processor. This is a reasonable amount of time for a research solution, but the process would probably need to be quicker for a forensic implementation. The individual slice reconstructions take up the vast majority of the time (more than 98%), fortunately this can be parallelised

over multiple processors or by utilising graphics processor hardware (Vaz et al., 2007; Mueller et al., 2007) and a significant speedup should occur.

Chapter 5

Conclusion and recommendations

5.1 Conclusion

It was shown that the Lodox Statscan could be used to produce tomographic reconstruction images, where the Lodox geometric measurements and c-arm angles required for reprojection were successfully acquired from image data. The top-of-image markers and the automated method for aligning the images in the scanning direction works as well as manual annotation and is robust and accurate to $\epsilon_{(top\text{-}of\text{-}image,\ max)} < 2$ pixels. The calibration markers and the automated method for detecting them works when the markers do not occlude one another or swap projection order (96% of the markers). Estimating the projected position of a marker is accurate to $\epsilon_{(calibration,\ max)} < 2$ pixels when it has been detected correctly.

Estimating the Lodox geometric configuration by minimizing the projection error of a set of three markers was regarded as successful as the overall reconstruction is successful.

The reprojection from Lodox fan beam geometry to orthogonal beam geometry produces image reconstructions where much of the anatomical detail present can be distinguished. Image quality, although tested to be inferior to a commercial CT scanner, shows promise for application within the forensic science facilities for cases where 3D images could provide insight before a post mortem dissection takes place.

The subsystem testing verified that marker positions are well estimated when correctly detected and also were useful in identifying the error cases and proved to be an aid in the identification of the cause of the failures. The reprojection based measures (reprojection error, normalised cross correlation and sinogram intensities) prove that projections of the reconstruction are similar to the original projections, but failed to provide value in identifying when the reconstruction was faulty, and are thus not considered good reconstruction metrics. The tests for 3D reconstruction accuracy and CT number consistency indicated that tomographic reconstruction was successful and that current reconstructions produced with the Lodox are inferior to the minimum standard for a medical CT scanner.

In conclusion, Lodox X-ray projections were acquired, features placed in the image were identified by a mostly-automatic set of image processing and an optimisation procedure estimated the Lodox Statscan geometric measurements and the c-arm angles, with which a projective transformation converted the Lodox fan beam data to orthogonal beam projections for use by MATLAB's implementation of the filtered back projection algorithm to successfully generate tomographic reconstruction images.

5.2   Recommendations

There are three categories of recommendations for future work:

Firstly, the calibration marker design needs to be refined to produce a completely robust automated solution for measuring the Lodox geometry and reprojecting to orthogonal data, and this should be tested more robustly, with multiple sets of manually annotated marker positions being compared to the automatically identified markers. Either the calibration marker hardware needs to be made such that there is no chance of the calibration markers occluding each other or the image processing method that identifies the calibration markers needs to be able to track the markers over the angular range of the image set to be able to predict and identify when projected markers occlude each other or swap position. The physical hardware for both top of image alignment and the system geometry and c-arm angles should be combined into a single device.

Secondly, investigation of different X-ray control techniques, back-projection filters and reconstruction resolution sizes is recommended to find optimal values. The X-ray control techniques used in this investigations were selected as convenient values that had been used previously for tomographic reconstruction (de Villiers, 2004), and the default back-projection filter of MATLAB's *iradon* function was used and an arbitrary reconstruction resolution and pixel size was selected. Performing studies where these parameters are varied should produce a configuration that allows for more useful reconstructions with better image quality.

Lastly, the operation of the Lodox Statscan needs to be modified to allow for automated image acquisition. The major restriction on using the Lodox Statscan for tomographic reconstruction is the completely manual method of image acquisition. Each projection must be scanned manually, to the degree that the scan-handle needs to be actuated for each image (Figure 2.4). The control system should also be rectified such that the top-of-image calibration is not required.

Bibliography

C. Bateman. New local scanners transform forensic pathology. *South African medical journal*, 98(2):75, 2008.

M.P. Beets. *Distortion Correction in LODOX StatScan X-Ray Images*. Master's thesis, University of Cape Town, 2007.

S. Beningfield, H. Potgieter, A. Nicol, S. Van As, G. Bowie, E. Hering, and E. Latti. Report on a new type of trauma full-body digital X-ray machine. *Emergency Radiology*, 10(1):23–29, 2003.

K.D. Boffard, J. Goosen, F. Plani, E. Degiannis, and H. Potgieter. The use of low dosage X-ray (Lodox/Statscan) in major trauma: comparison between low dose X-ray and conventional X-ray techniques. *The Journal of Trauma*, 60(6):1175, 2006.

S.A. Bolliger, M.J. Thali, S. Ross, U. Buck, S. Naether, and P. Vock. Virtual autopsy using imaging: bridging radiologic and forensic sciences. A review of the Virtopsy and similar projects. *European Radiology*, 18(2):273–282, 2008.

S.C. Bushong. *Computed tomography*. McGraw-Hill Medical, 2000. ISBN 0071343547.

Y. Cho, D.J. Moseley, J.H. Siewerdsen, and D.A. Jaffray. Accurate technique for complete geometric calibration of cone-beam computed tomography systems. *Medical physics*, 32:968, 2005.

EPA Constantino and KB Ozanyan. Sinogram recovery for sparse angle tomography using a sinusoidal Hough transform. *Measurement Science and Technology*, 19:094015, 2008.

M. de Villiers. *Limited angle tomography*. Master's thesis, University of Cape Town, 2000.

M. de Villiers. *Limited angle tomography*. PhD thesis, University of Cape Town, 2004.

J.T. Dobbins and D.J. Godfrey. Digital x-ray tomosynthesis: current state of the art and clinical potential. *Physics in medicine and biology*, 48(19):R65, 2003. ISSN 0031-9155.

E.L. Dove. Notes on computerized tomography. *Bioimaging Fundamentals*, 2001.

C.L. Epstein. *Introduction to the mathematics of medical imaging*. Society for Industrial and Applied Mathematics, 2008. ISBN 089871642X.

Q. Fang, S.A. Carp, R.H. Moore, D.B. Kopans, and D.A. Boas. Imaging Benign and Malignant Breast Lesions with Combined Optical Imaging and Tomosynthesis. In *Biomedical Optics*. Optical Society of America, 2010.

D.A. Forsyth and J. Ponce. *Computer vision: a modern approach*. Prentice Hall, 2002. ISBN 0130851981.

I.E. Gibb. Computed tomography of projectile injuries. *Clinical Radiology*, 63(10):1167–1168, 2008.

D.G. Grant. Tomosynthesis: A three-dimensional radiographic imaging technique. *Biomedical Engineering, IEEE Transactions on*, (1):20–28, 1972. ISSN 0018-9294.

G.T. Gullberg, B.M.W. Tsui, C.R. Crawford, and E.R. Edgerton. Estimation of geometrical parameters for fan beam tomography. *Physics in Medicine and Biology*, 32:1581, 1987.

R. Hartley and A. Zisserman. *Multiple view geometry in computer vision*. Cambridge University Press, 2003. ISBN 0521540518.

B.J. Irving, G.J Maree, E.R. Hering, and T.S. Douglas. Radiation dose from a linear slit scanning x-ray machine with full-body imaging capabilities. *Radiation protection dosimetry*, 130(4):482, 2008.

G.M. Israel, L. Cicchiello, J. Brink, and W. Huda. Patient size and radiation exposure in thoracic, pelvic, and abdominal ct examinations performed with automatic exposure control. *American Journal of Roentgenology*, 195(6):1342, 2010.

A.J. Jeffery, G.N. Rutty, C. Robinson, and B. Morgan. Computed tomography of projectile injuries. *Clinical Radiology*, 63(10):1160–1166, 2008.

A.C. Kak and M. Slaney. *Principles of computerized tomographic imaging*. 1999.

K. Kanaka, R.K. Samala, J. Zhang, and W. Qian. Reliability study of reconstruction methods in tomosynthesis imaging of various geometrical objects. In *Proceedings of SPIE*, volume 7622, page 762246, 2010.

G.J. Knobel, G. Flash, and G.F. Bowie. Lodox Statscan proves to be invaluable in forensic medicine. *Neurology*, 55:1075–1081, 2000.

Mathworks. Documentation, image processing toolbox, fanbeam. 2008.

Mathworks. Documentation, optimization toolbox, functions, least squares curve fitting, lsqnonlin. 2009.

M. Mitschke and N. Navab. Recovering the x-ray projection geometry for three-dimensional tomographic reconstruction with additional sensors: Attached camera versus external navigation system. *Medical Image Analysis*, 7(1):65–78, 2003.

K. Mueller, F. Xu, and N. Neophytou. Why do commodity graphics hardware boards (GPUs) work so well for acceleration of computed tomography? In *SPIE Electronic Imaging*, pages 1–12. Citeseer, 2007.

E.L. Nickoloff and P.O. Alderson. Radiation exposures to patients from ct: reality, public perception, and policy. *American Journal of Roentgenology*, 177(2):285, 2001.

F Nicolls. Geometric transformations for Lodox. Technical report, University of Cape Town, May 2010.

C. O'Donnell and N. Woodford. Post-mortem radiology—a new sub-speciality? *Clinical Radiology*, 63 (11):1189–1194, 2008.

D.L. Parker. Optimal short scan convolution reconstruction for fan beam ct. *Medical Physics*, 9:254, 1982.

H. Potgieter. The background, history and development of Lodox. Powerpoint presentation, February 2001.

K. Poulsen and J. Simonsen. Computed tomography as routine in connection with medico-legal autopsies. *Forensic Science International*, 171(2-3):190–197, 2007.

H.J. Teertstra, C.E. Loo, M.A.A.J. van den Bosch, H. van Tinteren, E.J.T. Rutgers, S.H. Muller, and K.G.A. Gilhuijs. Breast tomosynthesis in clinical practice: initial results. *European radiology*, 20(1): 16–24, 2010. ISSN 0938-7994.

M.J. Thali, C. Jackowski, L. Oesterhelweg, S.G. Ross, and R. Dirnhofer. VIRTOPSY—The Swiss virtual autopsy approach. *Legal Medicine*, 9(2):100–104, 2007.

Asser H. Thomsen, Anne Grethe Jurik, Lars Uhrenholt, and Annie Vesterby. An alternative approach to computerized tomography (CT) in forensic pathology. *Forensic Science International*, 183(1-3):87–90, 2009. ISSN 0379-0738.

C.L. Vaughan. Digital X-rays come of age. *South African Medical Journal*, 96(7):610, 2008.

M.S. Vaz, Y. Sneydersb, M. McLina, A. Rickera, and T. Kimpeb. GPU accelerated CT reconstruction for clinical use: quality driven performance. In *Proc. of SPIE Vol*, volume 6510, pages 65105G–1, 2007.